The Astrophysical Journal Supplement Series, 188:187–208, 2010 May doi:10.1088/0067-0049/188/1/187

BINARY NEUTRON STARS IN QUASI-EQUILIBRIUM

Keisuke Taniguchi[1,3] and Masaru Shibata[2]
[1] Department of Physics, University of Wisconsin-Milwaukee, P.O. Box 413, Milwaukee, WI 53201, USA
[2] Yukawa Institute for Theoretical Physics, Kyoto University, Kyoto 606-8502, Japan
Received 2009 December 31; accepted 2010 March 10; published 2010 April 30

ABSTRACT

Quasi-equilibrium sequences of binary neutron stars are constructed for a variety of equations of state in general relativity. Einstein's constraint equations in the Isenberg–Wilson–Mathews approximation are solved together with the relativistic equations of hydrostationary equilibrium under the assumption of irrotational flow. We focus on unequal-mass sequences as well as equal-mass sequences, and compare those results. We investigate the behavior of the binding energy and total angular momentum along a quasi-equilibrium sequence, the endpoint of sequences, and the orbital angular velocity as a function of time, changing the mass ratio, the total mass of the binary system, and the equation of state of a neutron star. It is found that the orbital angular velocity at the mass-shedding limit can be determined by an empirical formula derived from an analytic estimation. We also provide tables for 160 sequences, which will be useful as a guideline of numerical simulations for the inspiral and merger performed in the near future.

Key words: binaries: close – equation of state – stars: neutron

Online-only material: color figures, machine-readable table

1. INTRODUCTION

Coalescing binary neutron stars are among the most promising sources of gravitational waves for ground-based laser-interferometric gravitational-wave detectors such as LIGO (Brown et al. 2004), GEO600 (Lück et al. 2006), TAMA300 (Ando et al. 2005), and VIRGO (Acernese et al. 2007). Merger of binary neutron stars, together with that of black hole–neutron star binaries, is also considered to be one of the candidates for the central engines of short-hard gamma-ray bursts (Narayan et al. 1992). These facts motivate us to study coalescing binary neutron stars.

Binary neutron stars evolve as a result of gravitational radiation reaction and eventually merge. This evolutionary sequence is usually divided into three stages, depending on the characteristic timescales associated with orbital period and gravitational radiation reaction, as well as on the tidal effects for each neutron star. The first stage is the adiabatic, inspiral phase. In this phase, the timescale of orbital shrink due to the emission of gravitational waves is much longer than the orbital period, and thus, the binary system evolves adiabatically. In addition, each neutron star can be treated as a point mass, because the orbital separation is much larger than the neutron star radius and hence the tidal deformation of the neutron star is negligible. In this phase, a post-Newtonian approximation together with the point particle approximation is a robust tool for determining the orbital evolution and for computing gravitational waveforms (see, e.g., Blanchet 2006 and references therein).

The second stage is called the intermediate phase or the quasi-equilibrium phase. In this phase, the binary system is considered to be still in the adiabatic, inspiral phase, but we need to take into account tidal effects on each neutron star, i.e., hydrodynamic effects in neutron stars, as well as full effects of general relativity, because the orbital separation between two neutron stars is only a few times of the neutron star radius and thus they are in a strong two-body gravitational field. One of the aims of the present paper is to contribute to the understanding of this phase. We will explain more details about the purpose of the present paper later.

The last stage is the merger phase, for which the timescale of orbital shrink becomes shorter than the orbital period and thus the evolution of the system proceeds in a dynamical manner. Furthermore, the system becomes highly general relativistic, because the compactness of the system, defined by the ratio of the gravitational radius to the radius of the system, becomes larger than ~ 0.2. To clarify the merger phase, numerical relativity is the unique approach. Since the first fully general relativistic merger simulation was performed by Shibata (1999), huge effort has been devoted in this research field (Shibata & Uryū 2000, 2002; Shibata et al. 2003, 2005; Shibata & Taniguchi 2006; Duez et al. 2003; Miller et al. 2004; Anderson et al. 2008a, 2008b; Yamamoto et al. 2008; Liu et al. 2008; Baiotti et al. 2008; Giacomazzo et al. 2009; Kiuchi et al. 2009, 2010). (See, e.g., Oechslin & Janka 2007 and Oechslin et al. 2007 for works focusing on the micro-physics in a neutron star but not in fully general relativistic framework.)

Now we return to the intermediate phase and explain the purposes for studying the quasi-equilibrium phase of binary neutron stars in general relativity in detail. There are two roles for this study. One is to clarify the physical conditions in this phase, for example, how large the tidal deformation of a neutron star is, when the mass-shedding from the neutron star occurs, and what the orbital angular velocity at the mass-shedding limit is. The other is to provide initial data for studying the merger phase by numerical relativity simulations. Numerical relativity, in which Einstein's evolution equations are solved, requires initial data that satisfy Einstein's constraint equations and also that should be as physical as possible. Obviously, it is important to derive accurate initial data for a scientific study. Constructing such initial data is just obtaining relativistic binary neutron stars in quasi-equilibrium.

The first effort on this issue was devoted to constructing corotating binary neutron stars in general relativity because implementing a numerical code for computing such solutions is relatively easy (Baumgarte et al. 1997, 1998; Marronetti et al.

[3] Current address: Department of Earth Science and Astronomy, Graduate School of Arts and Sciences, University of Tokyo, Komaba, Meguro, Tokyo 153-8902, Japan.

1998; Usui et al. 2000; Usui & Eriguchi 2002; Taniguchi & Gourgoulhon 2002b, 2003; Tichy 2009). Kochanek (1992) and Bildsten & Cutler (1992), however, found that the timescale of coalescence driven by the gravitational-radiation reaction is much shorter than that of synchronization due to the viscosity in a neutron star. This implies that if the spin angular velocity of neutron stars is much smaller than the orbital angular velocity in a late inspiral phase, we can regard the rotation state of a neutron star to be approximately irrotational for the subsequent phase until the merger sets in. Additionally, any neutron star spins down due to electromagnetic radiation during its life from birth to the coalescence. The spin down timescale of a neutron star in a known binary is at longest as short as the coalescing timescale (larger than $\sim 10^8$ yr; Lorimer 2008). Moreover, the spin period of neutron stars in a known binary is always larger than 20 ms which is ~ 10 times larger than the orbital period in the late inspiral phase just prior to merger, 2–3 ms. Therefore, we can conclude that the irrotational flow is physically more realistic.[4]

Under the assumption of irrotation, formulation for solving relativistic hydrostatic equations was derived (Bonazzola et al. 1997; Asada 1998; Shibata 1998; Teukolsky 1998). Soon after the formulation was derived, quasi-equilibrium sequences of irrotational binary neutron stars were calculated (Bonazzola et al. 1999; Marronetti et al. 1999; Uryū & Eriguchi 2000; Uryū et al. 2000; Gourgoulhon et al. 2001; Taniguchi & Gourgoulhon 2002b, 2003; Bejger et al. 2005), based on the Isenberg–Wilson–Mathews (IWM) approximation to general relativity (Isenberg 1978, 2008; Wilson & Mathews 1989). (See Shibata et al. 2004 for an advanced formulation and Uryū et al. 2006, 2009 for the results.) Even though a lot of sequences have been, so far, calculated, systematic survey has not yet been done. In particular, *unequal-mass*, irrotational binary neutron stars with an *equation of state other than single polytrope* has not been studied in detail. In Taniguchi & Gourgoulhon (2002b, 2003), quasi-equilibrium sequences of unequal-mass binaries were calculated, but a polytropic equation of state (EOS) was used. In Bejger et al. (2005) and Uryū et al. (2009), non-polytropic EOSs were used, but quasi-equilibrium sequences of non-equal-mass binaries were not computed. Actually, unequal-mass, irrotational binary neutron stars with realistic EOSs in quasi-circular orbits were constructed and used as initial data for merger simulations in Shibata et al. (2005), Shibata & Taniguchi (2006), and Kiuchi et al. (2009, 2010).[5] We, however, have not constructed sequences, and rather computed only some initial data sets for each neutron star mass. The purpose of the present paper is to complete the issue and to provide a database of the sequences.

To compute unequal-mass binary systems of arbitrary mass ratio, we develop a new code for the present research, because the numerical code that we developed for the previous works (Taniguchi & Gourgoulhon 2002b, 2003) had a problem with calculating binary systems composed of significantly different-mass neutron stars in general relativity even though the problem was not in Newtonian computation (Taniguchi & Gourgoulhon 2002a). As we will explain in Section 2, the method to determine the center of mass of unequal-mass binary systems, i.e., the position of the rotation axis, caused the problem in the previous code, but we have overcome it by employing a new method.

In addition, we employ a wide variety of EOSs; piecewise polytropic EOSs (Read et al. 2009a, 2009b), tabulated realistic EOSs derived from nuclear physics, and fitted EOSs to the tabulated realistic EOSs. Some of the first and second EOSs were, respectively, used in Uryū et al. (2009) and in Bejger et al. (2005), but we adopt a wider set of EOSs in this paper. Furthermore, we systematically study the unequal-mass binaries, whereas Bejger et al. (2005) and Uryū et al. (2009) focused only on the equal-mass case.

This paper is organized as follows. We briefly review the basic equations and explain the improvement of the numerical code in Section 2. In Section 3, the results for the code test are shown. In Section 4, we show numerical results and discuss the effects of EOS on each sequence. Section 5 is devoted to a summary. Throughout this paper we adopt geometrized units with $G = c = 1$, where G denotes the gravitational constant and c the speed of light. Latin and Greek indices denote purely spatial and spacetime components, respectively.

2. FORMULATION

In this section, we briefly describe the basic equations to be solved and the method to calculate a quasi-equilibrium configuration in circular orbits. For more details, we would like to recommend readers to refer to Cook (2000), Baumgarte & Shapiro (2003), and Gourgoulhon (2007) for the part of gravitational field equations, and Gourgoulhon et al. (2001) for that of hydrostatic equations.

2.1. Gravitational Field Equations

The line element in 3+1 form is written as

$$\begin{aligned} ds^2 &= g_{\mu\nu}dx^\mu dx^\nu, \\ &= -\alpha^2 dt^2 + \gamma_{ij}(dx^i + \beta^i dt)(dx^j + \beta^j dt), \end{aligned} \tag{1}$$

where $g_{\mu\nu}$ is the spacetime metric, α is the lapse function, β^i is the shift vector, and γ_{ij} is the spatial metric induced on a spatial hypersurface Σ_t. Note here that the direction of the shift vector β^i is the normally used one which has a sign opposite to that used in Gourgoulhon et al. (2001) and Taniguchi & Gourgoulhon (2002b, 2003). The spatial metric γ_{ij} is further decomposed into the conformal factor ψ and a background metric $\tilde{\gamma}_{ij}$, and is written as

$$\gamma_{ij} = \psi^4 \tilde{\gamma}_{ij}. \tag{2}$$

The extrinsic curvature is defined by

$$K_{ij} = -\frac{1}{2}\mathcal{L}_n \gamma_{ij}, \tag{3}$$

where $\mathcal{L}_n$ is the Lie derivative along the unit normal to the hypersurface Σ_t. We split it into the trace K and the traceless part A_{ij} as

$$K_{ij} = A_{ij} + \frac{1}{3}\gamma_{ij}K. \tag{4}$$

We further rewrite the traceless part as

$$A_{ij} = \psi^{-2}\tilde{A}_{ij}, \tag{5a}$$

$$A^{ij} = \psi^{-10}\tilde{A}^{ij}, \tag{5b}$$

[4] If a first born neutron star in a binary was strongly recycled during the evolution of the companion, it may result in fast rotation and weak magnetic field. In such a case, the neutron star may rotate on the order of milliseconds even just before the merger. Some effort to approximately construct quasi-equilibrium, non-corotating, and non-irrotational binary systems is reported in Marronetti & Shapiro (2003) and Baumgarte & Shapiro (2009).

[5] We use the term "realistic equations of state" for the EOSs derived from nuclear physics, although no one really knows a realistic one.

where $\tilde{A}_{ij} = \tilde{\gamma}_{ik}\tilde{\gamma}_{jl}\tilde{A}^{kl}$. The Hamiltonian constraint, then, takes the form

$$\tilde{\nabla}^2\psi = -2\pi\psi^5\rho_H + \frac{1}{8}\psi\tilde{R} + \frac{1}{12}\psi^5 K^2 - \frac{1}{8}\psi^{-7}\tilde{A}_{ij}\tilde{A}^{ij}, \quad (6)$$

where $\tilde{\nabla}^2$ denotes $\tilde{\gamma}^{ij}\tilde{\nabla}_i\tilde{\nabla}_j$, $\tilde{\nabla}_i$ the covariant derivative with respect to $\tilde{\gamma}_{ij}$, and $\tilde{R}$ the scalar curvature with respect to $\tilde{\gamma}_{ij}$. The matter term, ρ_H, in Equation (6) is calculated by taking a projection of the stress–energy tensor. (See Equation (11) below.)

Equations (3), (4), and (5b) yield

$$\tilde{A}^{ij} = \frac{\psi^6}{2\alpha}\left(\partial_t\tilde{\gamma}^{ij} + \tilde{\nabla}^i\beta^j + \tilde{\nabla}^j\beta^i - \frac{2}{3}\tilde{\gamma}^{ij}\tilde{\nabla}_k\beta^k\right). \quad (7)$$

Using Equation (7) for the traceless part of the extrinsic curvature, the momentum constraint is written as

$$\begin{aligned}\tilde{\gamma}^{jk}\tilde{\nabla}_j\tilde{\nabla}_k\beta^i + \frac{1}{3}\tilde{\gamma}^{ik}\tilde{\nabla}_k(\tilde{\nabla}_j\beta^j) \\ = -\frac{\alpha}{\psi^6}\tilde{\nabla}_j\left(\frac{\psi^6}{\alpha}\partial_t\tilde{\gamma}^{ij}\right) + 16\pi\alpha\psi^4 j^i + \frac{4}{3}\alpha\tilde{\nabla}^i K \\ - \left(\tilde{\nabla}^i\beta^j + \tilde{\nabla}^j\beta^i - \frac{2}{3}\tilde{\gamma}^{ij}\tilde{\nabla}_k\beta^k\right)\frac{\alpha}{\psi^6}\tilde{\nabla}_j\left(\frac{\psi^6}{\alpha}\right), \quad (8)\end{aligned}$$

where the matter term, j^i, is calculated by taking a projection of the stress–energy tensor. (See Equation (12) below.) In addition to the Hamiltonian and momentum constraints, we solve the trace of the evolution equation of the extrinsic curvature

$$\begin{aligned}\partial_t K - \mathcal{L}_\beta K = -\psi^{-4}(\tilde{\nabla}_i\tilde{\nabla}^i\alpha + 2\tilde{\nabla}_i\ln\psi\tilde{\nabla}^i\alpha) \\ + \alpha\left[4\pi(\rho_H + S) + \psi^{-12}\tilde{A}_{ij}\tilde{A}^{ij} + \frac{K^2}{3}\right], \quad (9)\end{aligned}$$

where S is a matter term defined by Equation (14) below.

As mentioned, the matter terms in the above equations are calculated by taking the projections of the stress–energy tensor $T_{\mu\nu}$ into the spatial hypersurface Σ_t. In the present paper, we assume an ideal fluid and adopt the form of $T_{\mu\nu}$ as

$$T_{\mu\nu} = (\rho + \rho\epsilon + P)u_\mu u_\nu + P g_{\mu\nu}, \quad (10)$$

where u_μ is the fluid 4-velocity, ρ is the baryon rest-mass density, ϵ is the specific internal energy, and P is the pressure. Defining the future-directed unit normal to Σ_t as n_μ, the projections of $T_{\mu\nu}$ can be written as

$$\rho_H = n_\mu n_\nu T^{\mu\nu}, \quad (11)$$

$$j^i = -\gamma^i_\mu n_\nu T^{\mu\nu}, \quad (12)$$

$$S_{ij} = \gamma_{i\mu}\gamma_{j\nu}T^{\mu\nu}, \quad (13)$$

$$S = \gamma^{ij}S_{ij}. \quad (14)$$

The set of equations, (6)–(9), has four functions that we can choose freely; $\partial_t\tilde{\gamma}^{ij}$, $\partial_t K$, $\tilde{\gamma}_{ij}$, and K. For simplicity, we chose a maximal slicing $K = 0$ and adopt a flat metric $\tilde{\gamma}_{ij} = \eta_{ij}$ for the spatial background metric in the present paper. We then assume the presence of a helical Killing vector, ξ^μ, and the absence of gravitational waves in the wave zone. Under these assumptions, it is natural to choose the time direction so as to satisfy $\xi^\mu = (\partial/\partial t)^\mu$, and to set $\partial_t\tilde{\gamma}^{ij} = 0$ and $\partial_t K = 0$. Then, the basic equations are written as

$$\underline{\Delta}\psi = -2\pi\psi^5\rho_H - \frac{1}{8}\psi^{-7}\tilde{A}_{ij}\tilde{A}^{ij}, \quad (15)$$

$$\underline{\Delta}\beta^i + \frac{1}{3}\eta^{ik}\partial_k(\partial_j\beta^j) = 16\pi\Phi\psi^3 j^i + 2\tilde{A}^{ij}\partial_j(\Phi\psi^{-7}), \quad (16)$$

$$\underline{\Delta}\Phi = 2\pi\Phi\psi^4(\rho_H + 2S) + \frac{7}{8}\Phi\psi^{-8}\tilde{A}_{ij}\tilde{A}^{ij}, \quad (17)$$

$$\tilde{A}^{ij} = \frac{\psi^7}{2\Phi}\left(\eta^{ik}\partial_k\beta^j + \eta^{jk}\partial_k\beta^i - \frac{2}{3}\eta^{ij}\partial_k\beta^k\right), \quad (18)$$

where $\underline{\Delta}$ denotes the flat Laplacian, ∂_i the flat partial derivative, and $\Phi \equiv \alpha\psi$. The derived formulation is called the IWM approximation (Isenberg 1978, 2008; Wilson & Mathews 1989). Note here that a similar but more general formulation was recently proposed and started to be called the extended conformal thin-sandwich decomposition (XCTS; Pfeiffer & York 2003), mainly in the field of vacuum space time, i.e., black hole spacetime. In this new formulation, the conformal flatness is not assumed. (See Gourgoulhon 2007 for a more detailed explanation.)

It may be worthy to note that there is an effort to construct quasi-equilibrium binary neutron stars beyond the IWM approximation. Shibata et al. (2004) proposed a formalism in which all the Einstein equations are solved under the assumption of a helical Killing vector and artificially imposing asymptotic flatness. This formalism was used to solve quasi-equilibrium binary neutron stars in Uryū et al. (2006, 2009).

When solving the set of equations, (15)–(18), we need to impose the outer boundary conditions for ψ, β^i, and Φ. Because our numerical grids include spatial infinity by compactifying the outermost domain, we can impose the exact outer boundary conditions as

$$\psi = 1, \quad (19)$$

$$\beta^i = (\boldsymbol{\Omega}\times\boldsymbol{R})^i, \quad (20)$$

$$\Phi = 1, \quad (21)$$

where $\boldsymbol{\Omega}$ is the orbital angular velocity and $\boldsymbol{R}$ is the radial coordinate measured from the center of mass of the binary system. Although the shift vector seen by a co-orbiting observer, β^i, diverges at infinity, this diverging term,

$$\beta^i_{\rm rot} \equiv (\boldsymbol{\Omega}\times\boldsymbol{R})^i, \quad (22)$$

does not affect the set of equations we solve. If we define the shift vector seen by an inertial observer as $\beta^i_{\rm iner}$, the shift vector seen by a co-orbiting observer can be written as

$$\beta^i = \beta^i_{\rm iner} + \beta^i_{\rm rot}. \quad (23)$$

Because we have the relations,

$$\underline{\Delta}\beta^i_{\rm rot} = 0, \quad (24)$$

$$\partial_j\beta^j_{\rm rot} = 0, \quad (25)$$

and

$$\eta^{ik}\partial_k\beta^j_{\rm rot} + \eta^{jk}\partial_k\beta^i_{\rm rot} = 0, \tag{26}$$

substituting Equation (23) into Equations (16) and (18) yields

$$\Delta\beta^i_{\rm iner} + \frac{1}{3}\eta^{ik}\partial_k\left(\partial_j\beta^j_{\rm iner}\right) = 16\pi\Phi\psi^3 j^i + 2\tilde{A}^{ij}\partial_j(\Phi\psi^{-7}), \tag{27}$$

$$\tilde{A}^{ij} = \frac{\psi^7}{2\Phi}\left(\eta^{ik}\partial_k\beta^j_{\rm iner} + \eta^{jk}\partial_k\beta^i_{\rm iner} - \frac{2}{3}\eta^{ij}\partial_k\beta^k_{\rm iner}\right). \tag{28}$$

The outer boundary condition for $\beta^i_{\rm iner}$ is then $\beta^i_{\rm iner} = 0$ at spatial infinity. We actually solve for $\beta^i_{\rm iner}$.

2.2. Hydrostatic Equations

The hydrostatic equations governing the quasi-equilibrium state are the Euler and continuity equations. For both irrotational and synchronized motions, the Euler equation can be integrated once to give

$$h\alpha\frac{\gamma}{\gamma_0} = \text{constant}, \tag{29}$$

where $h = (\rho + \rho\epsilon + P)/\rho$ is the fluid specific enthalpy, γ_0 is the Lorentz factor between the co-orbiting and Eulerian observers, and γ is the Lorentz factor between the fluid and co-orbiting observers. If we define the 4-velocity of the co-orbiting observer by v^μ, the Lorentz factors are written as

$$\gamma_0 = -n^\mu v_\mu = \left(1 - \gamma_{ij}U^i_0 U^j_0\right)^{-1/2}, \tag{30}$$

$$\begin{aligned}\gamma &= -v^\mu u_\mu \\ &= \gamma_0\left(1 - \gamma_{ij}U^i U^j_0\right)(1 - \gamma_{ij}U^i U^j)^{-1/2},\end{aligned} \tag{31}$$

where U^i_0 is the orbital 3-velocity with respect to the Eulerian observer,

$$U^i_0 = \frac{\beta^i}{\alpha}, \tag{32}$$

and U^i denotes the fluid 3-velocity with respect to the Eulerian observer,

$$U^i = \frac{\psi^{-4}}{\alpha u^t h}\tilde{\nabla}^i\Psi, \tag{33}$$

for irrotational binary systems. Here u^t is the time component of the fluid 4-velocity and Ψ is the velocity potential which is calculated by solving the equation of continuity written as

$$\frac{\rho}{h}\nabla^\mu\nabla_\mu\Psi + (\nabla^\mu\Psi)\nabla_\mu\left(\frac{\rho}{h}\right) = 0, \tag{34}$$

where ∇_μ is the covariant derivative with respect to $g_{\mu\nu}$. Note that the fluid 3-velocity U^i corresponds to the orbital 3-velocity U^i_0 for synchronized binary systems.

For the determination of the constant on the right-hand side of Equation (29), we use the central value of the quantities on its left-hand side. The center of a neutron star is defined as the location of the maximum baryon rest-mass density in the present paper. Equation (29) includes one more constant which should be determined for each quasi-equilibrium figure; the constant is the orbital angular velocity as we find from Equations (32), (23), and (22). The method for calculating it will be explained in the next section.

2.3. Orbital Angular Velocity and the Center of Mass of a Binary System

The method for determining the orbital angular velocity is as follows: we first set the rotation axis of the binary system to be the Z-axis, and the line connecting the centers of mass of each neutron star to be the X-axis. Requiring a force balance along the X-axis, we impose a condition of quasi-circular orbit for the binary system. The force balance equation is obtained by setting the central values of the gradient of enthalpy to be zero for each star,

$$\left.\frac{\partial \ln h}{\partial X}\right|_{\mathcal{O}_a} = 0, \tag{35}$$

where $\mathcal{O}_a$ ($a = 1, 2$) denotes the center of each neutron star. Because Equation (29) includes Ω through Equation (22), the force balance Equation (35) may be regarded as the equation for determining the orbital angular velocity. Equation (35) also depends on the location of the center of mass, because Equation (22) includes $\boldsymbol{R}$ which is the radial coordinate measured from the center of mass of the binary system. For equal-mass binaries, the force balance equations for each star degenerate and the location of the center of mass becomes trivial, i.e., we can set it to the middle between two stars. For unequal-mass binaries, on the other hand, we have a couple of equations, Equation (35) for $a = 1$ and 2, for two parameters of the orbital angular velocity and the location of the center of mass. In the previous papers (Taniguchi & Gourgoulhon 2002b, 2003), those parameters were determined by solving the couple of equations as stated in Section II B of Taniguchi & Gourgoulhon (2002a). This method works for Newtonian binary systems (Taniguchi & Gourgoulhon 2002a) and also in the case that the difference in mass of the neutron stars is small for general relativistic binary systems. However, if the difference in mass of the neutron stars is significantly large, the coupled equations, Equation (35) for $a = 1$ and 2, would not be simultaneously satisfied at earlier steps of computational iteration because the state of the binary neutron stars is far from equilibrium, and as a result, the computation would fail to achieve the convergence to a solution.

To avoid such crush of computation for small mass ratios, $M^{\rm NS1}_{\rm ADM}/M^{\rm NS2}_{\rm ADM} < 0.8$ where $M^{\rm NSa}_{\rm ADM}(a = 1, 2)$ denotes the Arnowitt–Deser–Misner (ADM) mass for a spherical star a in isolation, we adopt the same method as used for black hole-neutron star binaries, described in Taniguchi et al. (2006, 2007, 2008), to determine the location of the center of mass; we require that the linear momentum of the system vanishes

$$P^i = \frac{1}{8\pi}\oint_\infty K^{ij}dS_j = 0. \tag{36}$$

Here we have assumed maximal slicing condition, $K = 0$. Once the location of the center of mass is determined in an iteration step, we move the position of each star, keeping the separation, in order for the center of mass of the binary system to locate on the Z-axis.

For the computation of the orbital angular velocity, we keep the method that Equation (35) is satisfied. As the readers may realize, Equation (35) gives two values of the orbital angular velocity for the unequal-mass case because there are two equations in Equation (35). Even though those values of the orbital angular velocity are very close (the relative difference is within the convergence level), they are slightly different because of numerical error. In the present paper, we just take an average of the two values.

It may be worthy to comment on another method for determining the orbital angular velocity. While our method for calculating Ω is to require the force balance Equation (35), it is possible to obtain Ω by requiring the enthalpy at two points on the neutron star's surface to be equal, i.e., $h = 1$ on the surface. We confirm that the results of those two methods coincide within the convergence level of the enthalpy.

2.4. Global Quantities and a Mass-shedding Indicator

A sequence of binary neutron stars should be constructed for a fixed baryon rest mass of each star,

$$M_{\rm B}^{(a)} = \int_{{\rm star}\,a} \rho u^t \sqrt{-g} d^3x, \quad a = 1, 2, \tag{37}$$

as the orbital separation decreases. This is because we regard the baryon rest mass as conserved as the orbital separation decreases due to the emission of gravitational waves. Along such a constant-baryon-rest-mass sequence, we then monitor three global quantities: the ADM mass, the Komar mass, and the total angular momentum, as well as a sensitive mass-shedding indicator of a star (see Equation (49)).

The ADM mass in isotropic Cartesian coordinates is written as

$$M_{\rm ADM} = -\frac{1}{2\pi} \oint_\infty \partial^i \psi dS_i. \tag{38}$$

If we use Equation (15) and Gauss' theorem, the ADM mass can be written in terms of volume integral as

$$M_{\rm ADM} = \int_V \left(\psi^5 \rho_H + \frac{1}{16\pi} \psi^{-7} \tilde{A}_{ij} \tilde{A}^{ij} \right) dV. \tag{39}$$

Both of Equations (38) and (39) give the same results relative to the convergence level of the computation.

The Komar mass is written as

$$M_{\rm Komar} = \frac{1}{4\pi} \oint_\infty \partial^i \alpha dS_i, \tag{40}$$

where we use the fact that the shift vector falls off rapidly enough to be neglected from Equation (40). Using the boundary conditions that $\Phi = 1$ and $\psi = 1$ at infinity and the definition $\Phi \equiv \alpha\psi$, we can rewrite Equation (40) as

$$M_{\rm Komar} = \frac{1}{4\pi} \oint_\infty (\partial^i \Phi - \partial^i \psi) dS_i. \tag{41}$$

Using Equations (15) and (17), the Komar mass can be also written in terms of volume integral as

$$M_{\rm Komar} = \frac{1}{4\pi} \int_V \Big[2\pi \psi^4 (\Phi + \psi) \rho_H + 4\pi \Phi \psi^4 S + \frac{1}{8} \psi^{-7} (7\Phi \psi^{-1} + 1) \tilde{A}_{ij} \tilde{A}^{ij} \Big] dV. \tag{42}$$

The total angular momentum of the binary system is calculated to give

$$J_i = \frac{1}{16\pi} \epsilon_{ijk} \oint_\infty (X^j K^{kl} - X^k K^{jl}) dS_l, \tag{43}$$

where X^i is a spatial Cartesian coordinate relative to the center of mass of the binary system. This equation can be also rewritten in the form of a volume integral as

$$J_i = \epsilon_{ijk} \int_V \psi^{10} X^j j^k dV, \tag{44}$$

where we use the momentum constraint equation. Similarly, the linear momentum (36) is written as

$$P^i = \int_V \psi^{10} j^i dV. \tag{45}$$

As we mentioned, both of the global quantities calculated by surface integral at infinity and by volume integral give the same results within the convergence level of the computation. In the present paper, we show the results by the volume integral.

The binding energy of the binary system is defined as

$$E_{\rm b} = M_{\rm ADM} - M_0, \tag{46}$$

where M_0 is the ADM mass of the binary system at infinite orbital separation, as defined by the sum of the ADM mass of two isolated neutron stars with the same baryon rest mass,

$$M_0 \equiv M_{\rm ADM}^{\rm NS1} + M_{\rm ADM}^{\rm NS2}. \tag{47}$$

To measure a global error in the numerical results, we define the error in the virial theorem as the fractional difference between the ADM and Komar masses,

$$\delta M \equiv \left| \frac{M_{\rm ADM} - M_{\rm Komar}}{M_{\rm ADM}} \right|. \tag{48}$$

We refer to δM as the virial error, and use it to measure the magnitude of numerical error in the ADM mass.

Finally, a sensitive mass-shedding indicator is defined as

$$\chi \equiv \frac{(\partial(\ln h)/\partial r)_{\rm eq}}{(\partial(\ln h)/\partial r)_{\rm pole}}. \tag{49}$$

Here, the numerator of Equation (49), $(\partial(\ln h)/\partial r)_{\rm eq}$, is the radial derivative of the enthalpy in equatorial plane at the surface along the direction toward the companion star, and the denominator, $(\partial(\ln h)/\partial r)_{\rm pole}$, is that at the surface of the pole. The radial coordinate r is measured from the center of the corresponding neutron star. For spherical stars at infinite separation, the indicator takes $\chi = 1$, while $\chi = 0$ indicates the formation of a cusp, and hence the onset of mass shedding. Note here that because our numerical code is based on a spectral method, it is impossible to construct cusp-like configurations, because it is accompanied by the Gibbs phenomena. This is also the case for the configuration with smaller values of $\chi \leqslant 0.5$. Thus, we stop constructing a sequence when χ reaches ~ 0.6.

2.5. Equations of State

In this section, we summarize four types of EOSs employed in this paper.

2.5.1. Polytropic EOSs

The first EOS is a polytrope

$$P = \kappa \rho^\Gamma, \tag{50}$$

where κ is a polytropic constant and Γ is the adiabatic index. This EOS has been often used in simply modeling binary neutron stars in quasi-equilibrium. We use this EOS only in testing our new code. The specific internal energy for the polytrope is written as

$$\epsilon = \frac{\kappa \rho^{\Gamma-1}}{\Gamma - 1}. \tag{51}$$

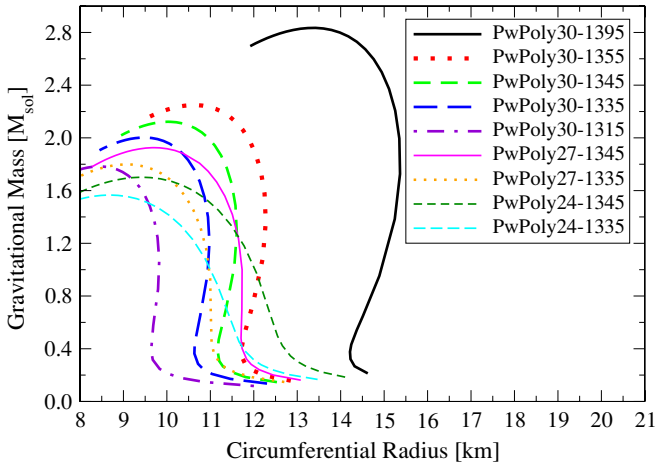

Figure 1. Mass–radius relation for spherical stars with piecewise polytropic EOSs. The vertical axis is the gravitational mass (which is the same as the ADM mass) in solar mass units and the horizontal axis is the circumferential radius in km units. The thick (black) solid, thick (red) dotted, thick (green) short-dashed, thick (blue) long-dashed, and thick (violet) dot-dashed curves denote the case of $\Gamma_1 = 3.0$ but $\log_{10} P_1 = 13.95$ (PwPoly30-1395), 13.55 (PwPoly30-1355), 13.45 (PwPoly30-1345), 13.35 (PwPoly30-1335), and 13.15 (PwPoly30-1315), respectively. The thin (magenta) solid and thin (orange) dotted curves are the case of $\Gamma_1 = 2.7$ but $\log_{10} P_1 = 13.45$ (PwPoly27-1345) and 13.35 (PwPoly27-1335), respectively. The thin (dark green) short-dashed and thin (cyan) long-dashed curves denote the case of $\Gamma_1 = 2.4$ but $\log_{10} P_1 = 13.45$ (PwPoly24-1345) and 13.35 (PwPoly24-1335), respectively.

(A color version of this figure is available in the online journal.)

For the polytropic EOS, we have the following natural units, i.e., polytropic units, to normalize the length, mass, and time scales:

$$R_{\rm poly} = \kappa^{1/(2\Gamma-2)}. \tag{52}$$

Because geometrized units with $G = c = 1$ are adopted, the polytropic units $R_{\rm poly}$ normalize all of the length, mass, and time scales.

2.5.2. Piecewise Polytropic EOSs

The second EOS is a piecewise polytrope introduced by Read et al. (2009a, 2009b). In the present paper, we set the number of polytrope segments to two. Then, the EOS is written as

$$P = \kappa_0 \rho^{\Gamma_0}, \quad (0 \leqslant \rho < \rho_0) \tag{53}$$

$$P = \kappa_1 \rho^{\Gamma_1}, \quad (\rho_0 \leqslant \rho), \tag{54}$$

where the dividing density ρ_0 is close to the nuclear density of order $\sim 10^{14}\,{\rm g\,cm^{-3}}$ (see below). The adiabatic index of the crust is set to a fixed value as $\Gamma_0 = 1.35692895$, whereas we choose three values for the adiabatic index of the core, $\Gamma_1 = 2.4$, 2.7, and 3.0. The polytropic constant of the crust, κ_0, is set to $\kappa_0/c^2 = 3.99873692 \times 10^{-8}(({\rm g\,cm^{-3}})^{1-\Gamma_0})$ in cgs units. The polytropic constant of the core, κ_1, is calculated by requiring the continuity of the pressure at the dividing density ρ_0 as

$$\kappa_1 = \kappa_0 \rho_0^{\Gamma_0 - \Gamma_1}. \tag{55}$$

The dividing density ρ_0 is calculated by setting the fiducial density, ρ_1, and the pressure at the fiducial density, P_1. We take the fiducial density as $\log_{10} \rho_1 = 14.7$ where ρ_1 is in cgs units. Because ρ_1 is larger than the dividing density ρ_0, the EOS has the form of $P_1 = \kappa_1 \rho_1^{\Gamma_1}$ at the fiducial density. Using this equation and Equation (55), the dividing density is obtained as

$$\log_{10} \rho_0 = \frac{\log_{10} P_1 - 14.7 \times \Gamma_1 - \log_{10} \kappa_0}{\Gamma_0 - \Gamma_1}. \tag{56}$$

The specific internal energy in the crust and that in the core are, respectively, written as

$$\epsilon_0 = \frac{\kappa_0 \rho^{\Gamma_0 - 1}}{\Gamma_0 - 1} \tag{57}$$

$$\epsilon_1 = a_1 + \frac{\kappa_1 \rho^{\Gamma_1 - 1}}{\Gamma_1 - 1}, \tag{58}$$

where a_1 is a constant which is calculated by requiring the continuity of the enthalpy at the dividing density ρ_0.

We summarize the adiabatic index of the core Γ_1, the logarithm of the pressure at the fiducial density $\log_{10} P_1$, the dividing density ρ_0, and the constant a_1 in Table 1; we employ nine parameter sets in the present work. Figure 1 plots the mass–radius relation of spherical stars for the chosen EOSs and indicates that a wide variety of EOSs are modeled.

Table 1
Parameters for the Piecewise Polytropic EOSs

Name	Γ_1	$\log_{10} P_1$	ρ_0 (g cm^{-3})	a_1
PwPoly30-1395	3.0	13.95	$7.03317468 \times 10^{13}$	$8.06036645 \times 10^{-3}$
PwPoly30-1355	3.0	13.55	$1.23196176 \times 10^{14}$	$9.84569621 \times 10^{-3}$
PwPoly30-1345	3.0	13.45	$1.41728987 \times 10^{14}$	$1.03506910 \times 10^{-2}$
PwPoly30-1335	3.0	13.35	$1.63049750 \times 10^{14}$	$1.08815874 \times 10^{-2}$
PwPoly30-1315	3.0	13.15	$2.15795830 \times 10^{14}$	$1.20264673 \times 10^{-2}$
PwPoly27-1345	2.7	13.45	$1.06888797 \times 10^{14}$	$9.00037733 \times 10^{-3}$
PwPoly27-1335	2.7	13.35	$1.26878530 \times 10^{14}$	$9.56832301 \times 10^{-3}$
PwPoly24-1345	2.4	13.45	$6.85371121 \times 10^{13}$	$7.24283128 \times 10^{-3}$
PwPoly24-1335	2.4	13.35	$8.54665331 \times 10^{13}$	$7.83658359 \times 10^{-3}$

2.5.3. Tabulated Realistic EOSs

We use tabulated EOSs for zero-temperature nuclear matter which are derived by using various theories of dense nuclear matter and different solution methods of the many-body problem in nuclear physics. As described in Bejger et al. (2005), the EOS of Baym et al. (1971) is used for $\rho < 10^8\,{\rm g\,cm^{-3}}$, that of Haensel & Pichon (1994) for $10^8\,{\rm g\,cm^{-3}} < \rho < 10^{11}\,{\rm g\,cm^{-3}}$, and that obtained by Douchin & Haensel (2001) for $10^{11}\,{\rm g\,cm^{-3}} < \rho < \rho_{\rm cc}$ in the neutron star crust, where $\rho_{\rm cc} = (0.6\text{–}1.4) \times 10^{14}\,{\rm g\,cm^{-3}}$ is the density at the crust–core interface. (See Chamel & Haensel 2008 for a review of the EOS in the neutron star crust.)

For the EOS of the neutron star core, we select six EOSs: APR (Akmal et al. 1998), BBB2 (Baldo et al. 1997), BPAL12 (Zuo et al. 1999), FPS (Friedman & Pandharipande 1981), GNH3 (Glendenning 1985), and SLy4 (Douchin & Haensel 2001). Those tabulated EOSs are interpolated by using the Hermite interpolation which is basically the same method as in Swesty (1996). Figure 2 shows the mass–radius relation for spherical stars in these EOSs.

2.5.4. Fitted EOSs to the Tabulated Realistic EOSs

The method of an interpolation for the tabulated realistic EOSs is not unique. Haensel & Potekhin (2005) introduced a fitting formula using an analytic function. We modified their method (Shibata et al. 2005) and derived a new fitting formula

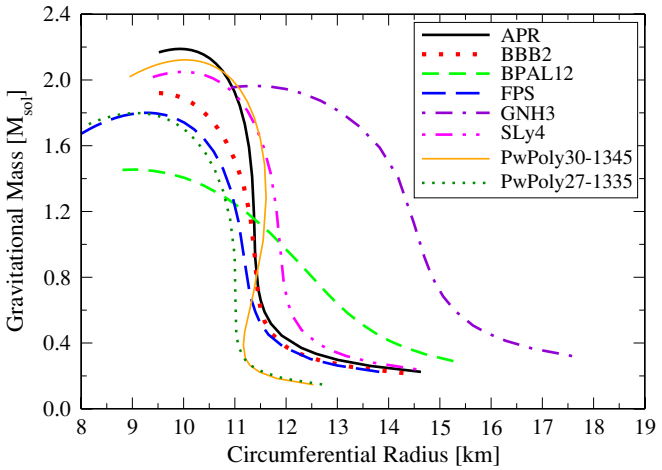

Figure 2. Same as Figure 1 but for tabulated realistic EOSs. The thick (black) solid, thick (red) dotted, thick (green) short-dashed, thick (blue) long-dashed, thick (violet) dot-dashed, and thick (magenta) dot-dot-dashed curves, respectively, denote the case of APR, BBB2, BPAL12, FPS, GNH3, and SLy4. The thin (orange) solid and thin (dark green) dotted curves are the case of piecewise polytropic EOSs with $\Gamma_1 = 3.0$ and $\log_{10} P_1 = 13.45$ (PwPoly30-1345) and $\Gamma_1 = 2.7$ and $\log_{10} P_1 = 13.35$ (PwPoly27-1335). Those curves are shown for comparison.

(A color version of this figure is available in the online journal.)

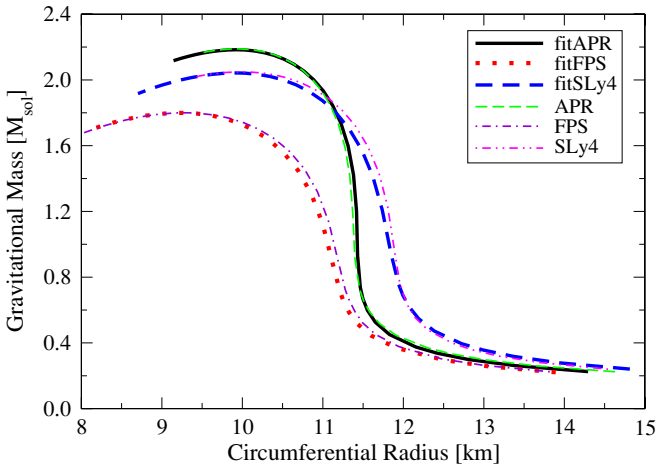

Figure 3. Same as Figure 1 but for EOSs written by a fitting formula. The thick (black) solid, thick (red) dotted, and thick (blue) short-dashed curves denote the case of fitAPR, fitFPS, and fitSLy4, respectively. The thin (green) long-dashed, thin (violet) dot-dashed, and thin (magenta) dot-dot-dashed curves are the case of tabulated EOSs, APR, FPS, and SLy4, respectively.

(A color version of this figure is available in the online journal.)

for FPS and SLy4 to satisfy the first law of thermodynamics. In Shibata & Taniguchi (2006), we also derived a fitting formula for APR. In the present paper, we construct quasi-equilibrium sequences for those EOSs, fitAPR, fitFPS, and fitSLy4, and compare the results with those by the tabulated EOSs.

Figure 3 compares the mass–radius relation for spherical stars with those by the tabulated EOSs, APR, FPS, and SLy4. A good agreement is found between two corresponding results for each EOS.

3. CODE TESTS

We implemented a new numerical code based on the spectral method library, LORENE, developed by the Meudon relativity group. (See the LORENE Web site, http://www.lorene.obspm.fr/, for more detailed explanations of this code library.) Our new numerical code was tested to check its ability for accurately computing unequal-mass binary systems composed of significantly different-mass neutron stars as well as equal-mass ones with similar accuracy to those obtained by the old code used in Gourgoulhon et al. (2001), Taniguchi & Gourgoulhon (2002b, 2003), and Bejger et al. (2005).

3.1. Convergence Tests

The first test is to check if the convergence of the ADM mass of an equal-mass binary neutron star is achieved with increasing the resolution. We choose the $\Gamma = 2$ polytrope and set the baryon rest mass of each star to $\bar{M}_{\rm B} = 0.15$ in polytropic units. Two different orbital separations, $\bar{d} = 7.308$ and 3.045 in polytropic units, are chosen. Those coordinate separations are, respectively, about 8.965 and 3.736 times larger than the coordinate radius of an isolated, spherical neutron star with the same baryon rest mass. We choose these separations because the former one, $d/a_{\rm NS} = 8.965$, is larger than the farthest separation in the equal-mass sequences we show in the present paper ($d/a_{\rm NS} \sim 8.6$) and the latter one, $d/a_{\rm NS} = 3.736$, is an intermediate separation between the farthest and the closest ones.

Figures 4 and 5 compare the ADM mass at $\bar{d} = 7.308$ and 3.045, respectively, for different resolutions (for different number of collocation points in the terminology of the spectral method). We choose five resolutions, $N_r \times N_\theta \times N_\phi = 49 \times 37 \times 36$, $41 \times 33 \times 32$, $33 \times 25 \times 24$, $25 \times 17 \times 16$, and $21 \times 13 \times 12$, where N_r, N_θ, and N_ϕ denote the number of collocation points for the radial, polar, and azimuthal directions, respectively. The horizontal axis of these figures denotes the cube root of the total number of collocation points, $\sqrt[3]{N_r \times N_\theta \times N_\phi}$. The error bar is drawn for an estimated error size derived from the virial error.

It is found from Figure 4 that the ADM mass for $41 \times 33 \times 32$ ($\sqrt[3]{N_r \times N_\theta \times N_\phi} \simeq 35.11$) is in approximately convergent level because its value is approximately identical to that for $49 \times 37 \times 36$ ($\sqrt[3]{N_r \times N_\theta \times N_\phi} \simeq 40.26$). The central value of the ADM mass for $33 \times 25 \times 24$ ($\sqrt[3]{N_r \times N_\theta \times N_\phi} \simeq 27.05$) is in the error bar of that for $49 \times 37 \times 36$. This implies that the number of collocation points, $33 \times 25 \times 24$, is sufficiently large when computing the binary with smaller separations than $d/a_{\rm NS} \sim 9.0$ within the fractional error of 10^{-5} for the ADM mass, which satisfies the required accuracy in our present computation.

Figure 5 shows that the ADM mass for $33 \times 25 \times 24$ is in approximately convergent level because its value is approximately identical to that for $49 \times 37 \times 36$ at the separation of $\bar{d} = 3.045$ ($d/a_{\rm NS} = 3.736$). The central value for $25 \times 17 \times 16$ ($\sqrt[3]{N_r \times N_\theta \times N_\phi} \simeq 18.95$) is in the error bar of that for $49 \times 37 \times 36$. This implies that it is safe to decrease the number of collocation points for smaller separations than $d/a_{\rm NS} \sim 3.7$ within the accuracy required in the present computation.

From these convergence tests, we decide to use the number of collocation points of $N_r \times N_\theta \times N_\phi = 33 \times 25 \times 24$ for larger separations and $33 \times 17 \times 16$ for closer ones, keeping the number of collocation points for the radial direction.

3.2. An Unequal-mass Binary System Composed of Significantly Different-mass Stars

To illustrate that our new code can compute a binary system composed of significantly different-mass stars, we show in Figure 6 a quasi-equilibrium configuration of binary neutron

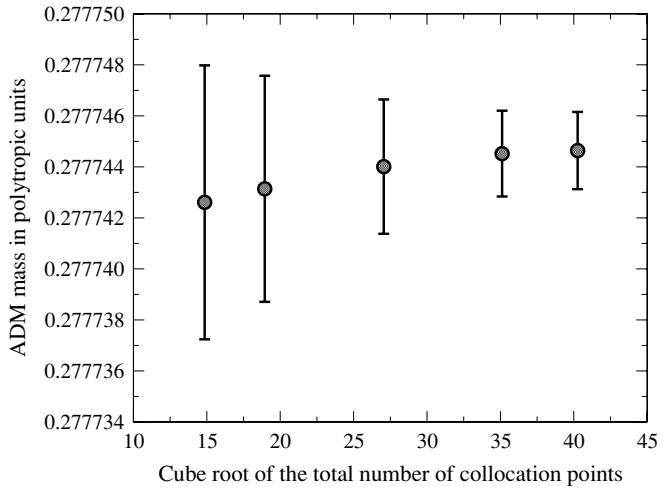

Figure 4. Convergence test of the ADM mass of a binary neutron star with the $\Gamma = 2$ polytropic EOS. The baryon rest mass of each star is $\bar{M}_{\rm B} = 0.15$ and the coordinate orbital separation is set to $\bar{d} = 7.308$ ($d/a_{\rm NS} = 8.965$). The horizontal axis denotes the cube root of the total number of collocation points. The filled circles are the central value of each computation, and the error bars are drawn for an estimated error size derived from the virial error.

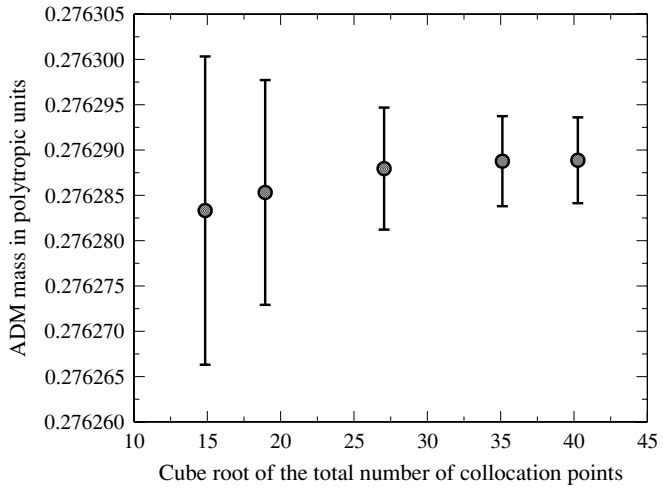

Figure 5. Same as Figure 4 but for the coordinate, orbital separation of $\bar{d} = 3.045$ ($d/a_{\rm NS} = 3.736$).

stars with the $\Gamma = 2$ polytrope whose baryon rest masses are $\bar{M}_{\rm B} = 0.05$ and 0.15, respectively. The compactness of those stars when they have a spherical shape is, respectively, $\mathcal{C} \equiv M^{\rm NS}_{\rm ADM}/R_{\rm NS} = 0.04155$ and 0.1452, where $R_{\rm NS}$ is the circumferential radius. Because the maximum baryon rest mass of the $\Gamma = 2$ polytrope is $\bar{M}_{\rm B} \approx 0.18$, the model of $\bar{M}_{\rm B} = 0.05$ is an extremely light neutron star. We compute this model just to demonstrate the ability of our code. In the figure, the star on the left-hand side has $\bar{M}_{\rm B} = 0.05$ and that on the right-hand side does 0.15. The thick solid circles are the location of the neutron star's surface. The orbital angular velocity, the binding energy, the total angular momentum, the virial error, and the linear momentum of this figure are $M_0\Omega = 5.218 \times 10^{-3}$, $E_{\rm b}/M_0 = -2.816 \times 10^{-3}$, $J/M_0^2 = 1.1626$, $\delta M = 2.027 \times 10^{-6}$, and $P^Y/(M_0 c) = 3.930 \times 10^{-7}$, respectively. The relative difference of the binding energy from that obtained by the third post-Newtonian (3PN) approximation at the same orbital angular

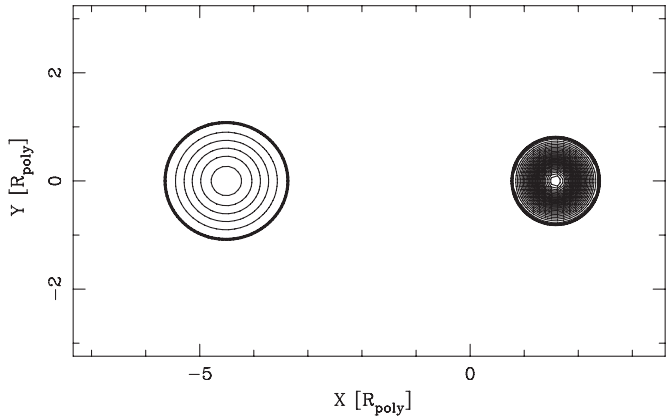

Figure 6. Contours of baryon rest-mass density for demonstrating the ability of constructing a quasi-equilibrium figure composed of significantly different-mass stars. The EOS we employ is the $\Gamma = 2$ polytrope. The star on the left-hand side has the baryon rest mass of $\bar{M}_{\rm B} = 0.05$, while that on the right-hand side has $\bar{M}_{\rm B} = 0.15$. The thick solid circles are the location of stellar surface.

velocity is about $\delta E_{\rm b} = -6.479 \times 10^{-4}$. Here we define

$$\delta E_{\rm b} \equiv \frac{(E_{\rm b})_{\rm num}}{(E_{\rm b})_{\rm 3PN}} - 1, \tag{59}$$

where $(E_{\rm b})_{\rm num}$ and $(E_{\rm b})_{\rm 3PN}$ denote the binding energy obtained by the numerical computation and that by the 3PN approximation, respectively. The relative difference of the total angular momentum from that obtained by the 3PN approximation at the same orbital angular velocity is $\delta J = -1.693 \times 10^{-4}$, defining δJ similar to Equation (59). The relative error in baryon rest mass of the less massive star is $\delta \bar{M}_{\rm B} = 6.738 \times 10^{-7}$ and that of the more massive star is 2.082×10^{-6}. We do not find any problem to accurately construct a binary system composed of two significantly different-mass neutron stars.

3.3. Comparison with the Results Obtained by the Old Code

We compare the linear momentum of an unequal-mass binary neutron star along a quasi-equilibrium sequence for a model of piecewise polytrope (PwPoly30-1345) with masses of $M^{\rm NS1}_{\rm ADM} = 1.25\,M_\odot$ and $M^{\rm NS2}_{\rm ADM} = 1.45\,M_\odot$ in Figure 7. This figure compares the linear momentum of the Y-component, where we assume that the centers of mass of the neutron stars are located on the X-axis (see Figure 6 about the location of each star). This shows that the present results give by more than two orders smaller values than those calculated by the old code through the sequence. This improvement results from the change in the solution method of the center of mass for achieving a convergence. Note that the linear momentum of the X- and Z-directions is zero within the machine precision because of the imposed symmetries.

We also compare the relative difference of the binding energy from that obtained by the 3PN approximation in Figure 8. The definition of the relative difference is shown in Equation (59). The (black) solid curve with the filled circles denotes the results calculated by the new code, and the (red) dashed curve with the open squares is those computed by the old code. The error bar is drawn for an estimated error size derived from the virial error. It is found from Figure 8 that the results by the new code have a factor of 2–5 smaller error bar than those by the old code except for very close separations ($M_0\Omega > 0.037$). Additionally, when we used the old code, we could not compute sufficiently converged figures for larger separations ($M_0\Omega < 0.017$),

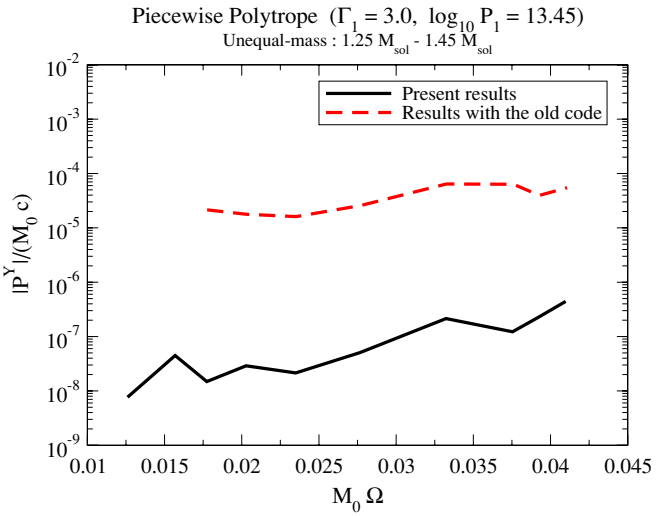

Figure 7. Comparison of the linear momentum along a quasi-equilibrium sequence of an unequal-mass binary composed of $M_{\rm ADM}^{\rm NS1} = 1.25\,M_\odot$ and $M_{\rm ADM}^{\rm NS2} = 1.45\,M_\odot$ stars. The EOS we select is the piecewise polytrope with $\Gamma_1 = 3.0$ and $\log_{10} P_1 = 13.45$ (PwPoly30-1345). The thick (black) solid curve denotes the results calculated by our new code while the thick (red) dashed one is those calculated by the old code.

(A color version of this figure is available in the online journal.)

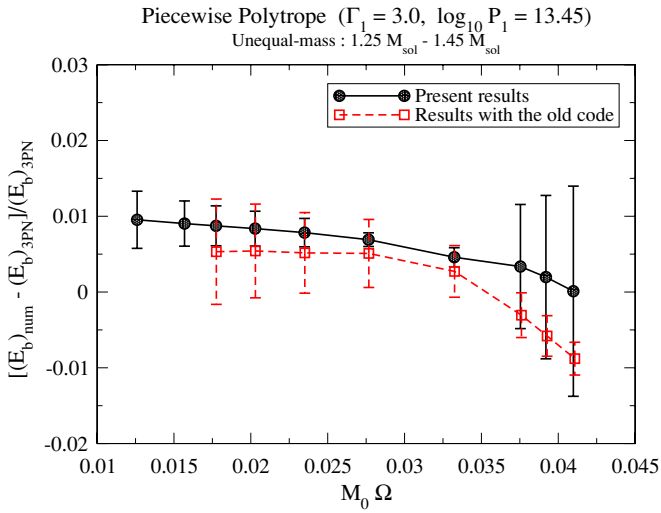

Figure 8. Comparison of the relative difference of the numerically obtained binding energy from that by the 3PN approximation along the same quasi-equilibrium sequence in Figure 7. The (black) solid curve with filled circles denotes the relative difference of the binding energy calculated by our new code, and the (red) dashed curve with open squares is that computed by the old code. The error bar is drawn for an estimated error size derived from the virial error.

(A color version of this figure is available in the online journal.)

because the code fails to correctly determine the center of mass during the computational iterations. For smaller mass ratio than the model shown in Figure 8, $M_{\rm ADM}^{\rm NS1}/M_{\rm ADM}^{\rm NS2} \simeq 0.862$, the old code also fails to achieve the convergence, because the code crushes at earlier steps of computational iteration.

We conclude that our new code gives results as accurate as those obtained by the old code. In addition, it can compute models with smaller mass ratios that the old code cannot.

4. NUMERICAL RESULTS

Quasi-equilibrium sequences for 18 EOSs are computed, choosing three total masses, $M_0 = 2.4\,M_\odot$, $2.7\,M_\odot$, and $3.0\,M_\odot$, and three mass ratios for each total mass. The computation is performed with the collocation points of $N_r \times N_\theta \times N_\phi = 33 \times 25 \times 24$ for larger separations and $33 \times 17 \times 16$ for closer ones. The number of domains which cover the computational region around each star is six for larger separations and five for closer ones. The results are summarized in Appendix B.

4.1. Contours of Baryon Rest-mass Density

Figures 9–12 show contours of baryon rest-mass density for 4 EOSs in the equatorial plane. Masses of the stars on the left- and right-hand sides are $M_{\rm ADM}^{\rm NS1} = 1.15\,M_\odot$ and $M_{\rm ADM}^{\rm NS2} = 1.55\,M_\odot$, respectively. All the figures are drawn for the closest separation that we can choose. The *X*- and *Y*-axes are measured by the coordinate length in km units. Figure 9 is for the tabulated EOS of APR and Figure 10 is for that of GNH3. The former EOS gives relatively compact stars, while the latter one produces rather less compact stars. Figures 11 and 12 are selected among the EOSs of piecewise polytrope, PwPoly30-1345 and PwPoly24-1345. Both of the piecewise polytropes produce stars of a similar size for a given mass, $M_{\rm ADM}^{\rm NS} \simeq 1.3\,M_\odot$, but the former model, PwPoly30-1345, has a stiff EOS for the core ($\Gamma_1 = 3.0$) while the latter one, PwPoly24-1345, has a soft EOS ($\Gamma_1 = 2.4$). This difference in Γ_1 is reflected strongly in the structure of more massive star for which the central density is high and the effect

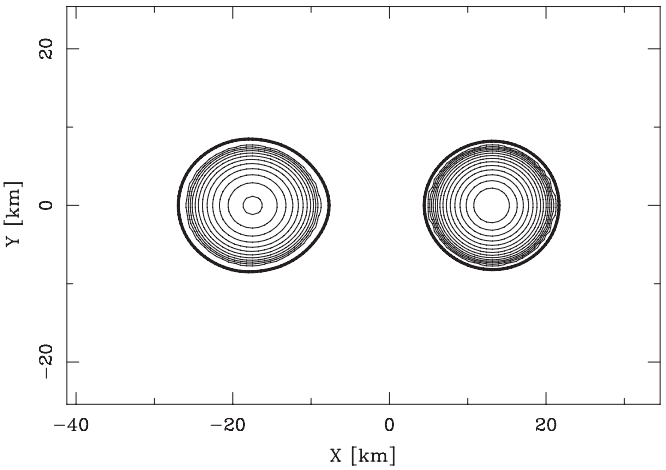

Figure 9. Contours of baryon rest-mass density for the EOS of APR. The star on the left-hand side has $M_{\rm ADM}^{\rm NS1} = 1.15\,M_\odot$ while that on the right-hand side does $M_{\rm ADM}^{\rm NS2} = 1.55\,M_\odot$. The thick solid circles denote the location of stellar surface. The axes are the coordinate length in km units.

of Γ_1 is appreciated. By contrast, a striking difference is not seen for the less massive star.

4.2. Binding Energy and Total Angular Momentum

Figure 13 shows the binding energy of quasi-equilibrium sequences for five piecewise polytropic EOSs. Those sequences are calculated for binary neutron stars composed of equal-mass stars of $M_{\rm ADM}^{\rm NS1} = M_{\rm ADM}^{\rm NS2} = 1.35\,M_\odot$. All of the piecewise polytropes we select here have $\Gamma_1 = 3.0$, but the value of $\log_{10} P_1$ varies from 13.95 to 13.15. The thick (red) short-dashed, thick (green) long-dashed, thick (blue) dot-dashed, thick (violet) dot-dot-dashed, and thick (magenta) dot-dash-dashed curves denote, respectively, the results for $\log_{10} P_1 = 13.95$ (PwPoly30-1395), 13.55 (PwPoly30-1355), 13.45 (PwPoly30-1345), 13.35 (PwPoly30-1335), and 13.15 (PwPoly30-1315). The thin (black) solid curve denotes the

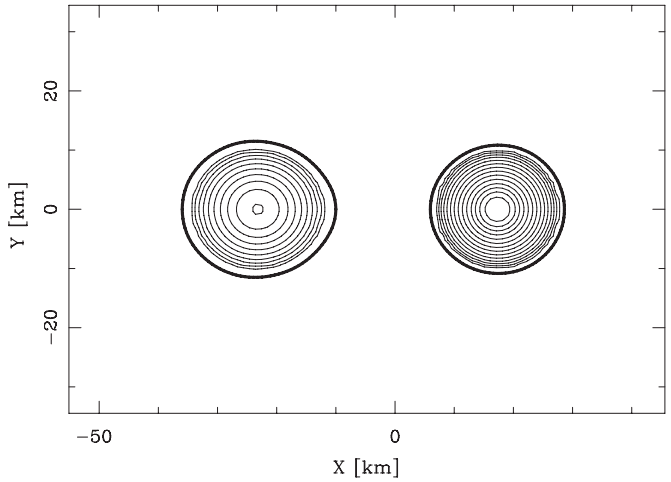

Figure 10. Same as Figure 9 but for the EOS of GNH3.

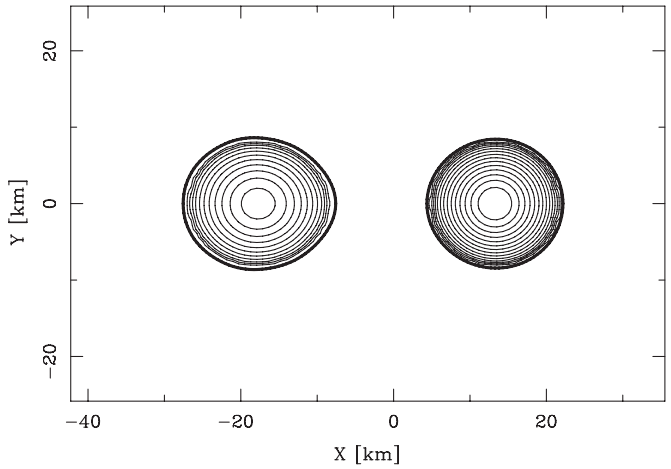

Figure 11. Same as Figure 9 but for the EOS of PwPoly30-1345.

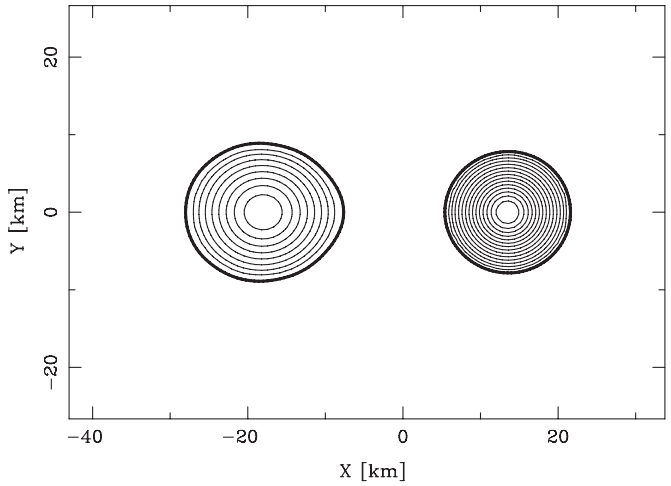

Figure 12. Same as Figure 9 but for the EOS of PwPoly24-1345.

results in the 3PN approximation. The total angular momentum for the same EOSs is also plotted in Figure 14. The sequences are terminated just before the stars reach the mass-shedding limit, because the spectral method we use has a problem in handling a cusp-like figure. We will discuss the endpoint in detail in Section 4.3.

Figure 13 shows that the orbital angular velocity at the closest separation increases from $M_0\Omega \simeq 0.029$ to $\simeq 0.056$ as the value

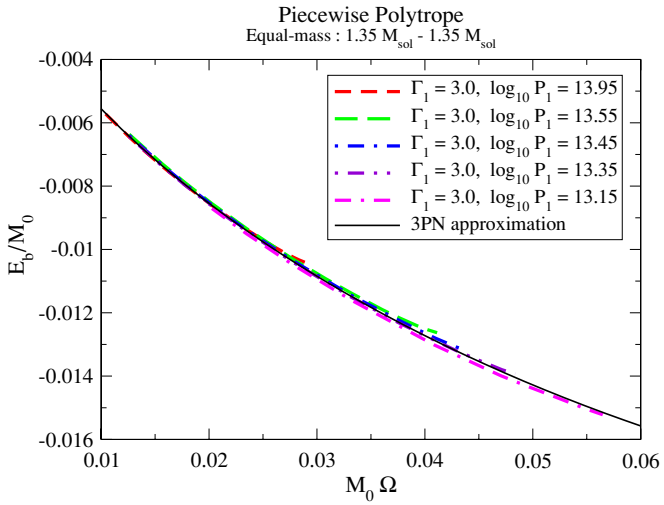

Figure 13. Binding energy along a quasi-equilibrium sequence of an equal-mass binary neutron star as a function of the orbital angular velocity. Each ADM mass of the neutron stars is set to 1.35 $M_\odot$ at infinite separation. The EOSs are the piecewise polytrope with $\Gamma_1 = 3.0$. The thick (red) short-dashed, thick (green) long-dashed, thick (blue) dot-dashed, thick (violet) dot-dot-dashed, and thick (magenta) dot-dash-dashed curves are, respectively, the cases of $\log_{10} P_1 = 13.95$ (PwPoly30-1395), 13.55 (PwPoly30-1355), 13.45 (PwPoly30-1345), 13.35 (PwPoly30-1335), and 13.15 (PwPoly30-1315). The thin (black) solid curve denotes the results of the 3PN approximation.

(A color version of this figure is available in the online journal.)

of $\log_{10} P_1$ decreases from 13.95 to 13.15. Because the model with $\log_{10} P_1 = 13.95$ (PwPoly30-1395) has the largest radius for a spherical neutron star among the models in Figure 13, the effect of tidal deformation is the largest. We understand this behavior with the help of a Newtonian analytic estimation as follows: by equating the gravity of a neutron star (NS1) attracting on a test mass on the neutron star's surface with the tidal force of the companion neutron star (NS2) attracting on the test mass, we obtain the separation at which the mass-shedding will occur for NS1. The separation is written in the form

$$\frac{d_{\rm ms}}{r_{\rm NS1}} = A\left(\frac{M_{\rm NS2}}{M_{\rm NS1}}\right)^{1/3}, \tag{60}$$

where A, $r_{\rm NS1}$, $M_{\rm NS1}$, and $M_{\rm NS2}$ denote a constant of order unity, the NS1's radius, the NS1's mass, and the NS2's mass, respectively. Eliminating the separation at the mass-shedding from the Keplerian angular velocity $\Omega = \sqrt{(M_{\rm NS1} + M_{\rm NS2})/d_{\rm ms}^3}$, we have

$$M_{\rm tot}\Omega = \left(\frac{M_{\rm tot}}{A r_{\rm NS1}}\right)^{3/2}\left(\frac{M_{\rm NS1}}{M_{\rm NS2}}\right)^{1/2}, \tag{61}$$

where $M_{\rm tot} \equiv M_{\rm NS1} + M_{\rm NS2}$ is the total mass. Taking the ratio of the orbital angular velocity at the mass-shedding for PwPoly30-1395 to that for PwPoly30-1315, we obtain

$$\frac{(M_{\rm tot}\Omega)_{1395}}{(M_{\rm tot}\Omega)_{1315}} = \left(\frac{r_{\rm NS1}^{1315}}{r_{\rm NS1}^{1395}}\right)^{3/2}. \tag{62}$$

Noting that the masses are $M_{\rm NS1} = M_{\rm NS2} = 1.35\,M_\odot$ and $r_{\rm NS1}$ is the circumferential radius, we have the ratio as 0.51 from Table 2. This value agrees approximately with the obtained ratio of the orbital angular velocity at the closest separation,

$$\frac{(M_0\Omega)_{1395}}{(M_0\Omega)_{1315}} \simeq \frac{0.029}{0.056} \simeq 0.52. \tag{63}$$

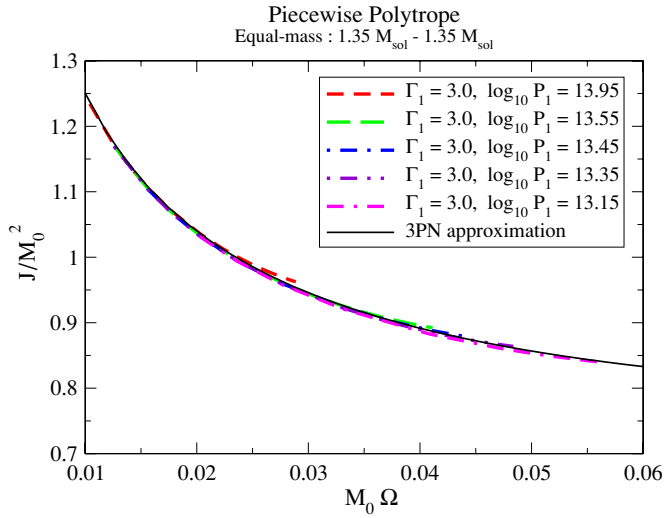

Figure 14. Same as Figure 13 but for the total angular momentum.
(A color version of this figure is available in the online journal.)

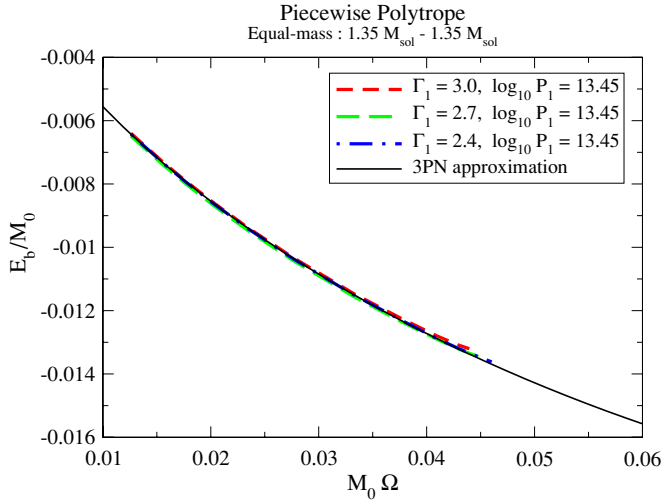

Figure 15. Same as Figure 13 but for the piecewise polytrope with $\log_{10} P_1 = 13.45$. The thick (red) short-dashed, thick (green) long-dashed, and thick (blue) dot-dashed curves denote the cases with the adiabatic index of $\Gamma_1 = 3.0$ (PwPoly30-1345), 2.7 (PwPoly27-1345), and 2.4 (PwPoly24-1345), respectively. The thin (black) solid curve denotes the results of the 3PN approximation.
(A color version of this figure is available in the online journal.)

As a result of the smaller orbital angular velocity at the closest separation, the model with $\log_{10} P_1 = 13.95$ (PwPoly30-1395) has the nondimensional angular momentum as large as $J/M_0^2 \sim 0.96$, as shown in Figure 14. By contrast, the most compact model with $\log_{10} P_1 = 13.15$ (PwPoly30-1315) has $J/M_0^2 \sim 0.84$, much smaller than 0.96, because the binary system can come closer than that composed of less compact stars. These differences suggest that the merger process will depend strongly on the EOS: for the stiffer EOS, the nondimensional angular momentum at the onset of merger may be too large to form a black hole soon, whereas for the softer EOS, it may be small enough that the merged object collapses to a black hole in a dynamical timescale ~ 1 ms.

Figure 15 is drawn for the binding energy of equal-mass binary neutron stars with $M_{\rm ADM}^{\rm NS1} = M_{\rm ADM}^{\rm NS2} = 1.35\,M_\odot$. The chosen EOSs are the piecewise polytrope with a fixed value of $\log_{10} P_1 = 13.45$, but the value of Γ_1 is varied from 3.0 to 2.4.

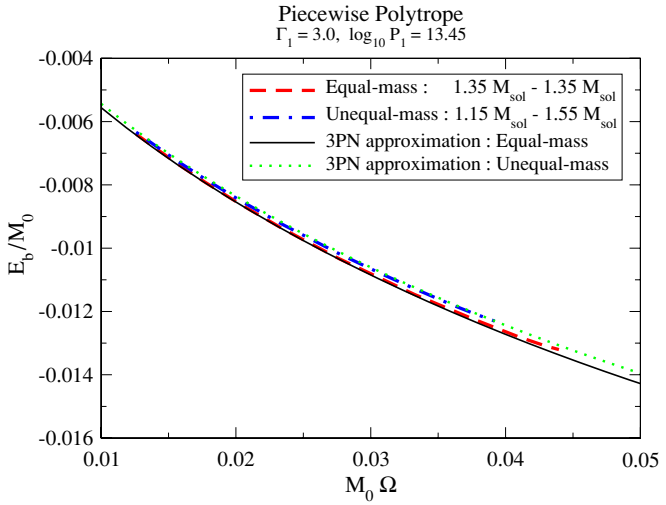

Figure 16. Same as Figure 13 but for comparing the results of equal-mass binary neutron stars with those of unequal-mass ones. The EOS is the piecewise polytrope with $\Gamma_1 = 3.0$ and $\log_{10} P_1 = 13.45$ (PwPoly30-1345). The thick (red) dashed curve denotes the case of an equal-mass binary with $M_{\rm ADM}^{\rm NS1} = M_{\rm ADM}^{\rm NS2} = 1.35\,M_\odot$, while the thick (blue) dot-dashed one is the case of an unequal-mass binary composed of $M_{\rm ADM}^{\rm NS1} = 1.15\,M_\odot$ and $M_{\rm ADM}^{\rm NS2} = 1.55\,M_\odot$ stars. The thin (black) solid and thin (green) dotted curves are the results of the 3PN approximation for equal-mass and unequal-mass binaries, respectively.
(A color version of this figure is available in the online journal.)

The thick (red) short-dashed, thick (green) long-dashed, and thick (blue) dot-dashed curves denote the results for $\Gamma_1 = 3.0$ (PwPoly30-1345), 2.7 (PwPoly27-1345), and 2.4 (PwPoly24-1345), respectively. For these three models, the radius of a spherical star for $M_{\rm ADM}^{\rm NS} = 1.35\,M_\odot$ has almost the same value but very slightly more compact for $\Gamma_1 = 2.4$ than for $\Gamma_1 = 3.0$ (see Figure 1 and Table 2). It is found that the orbital angular velocity at the closest separation increases from $M_0\Omega \simeq 0.044$ to 0.046 as the adiabatic index of the neutron star core is decreased from $\Gamma_1 = 3.0$ to 2.4. This variation of the orbital angular velocity is smaller than that by the change of $\log_{10} P_1$ as seen in Figure 13. This implies that for neutron stars of mass $1.35M_\odot$, the variation in $\log_{10} P_1$, which affects the stellar radius, results in a larger effect on the determination of the orbital angular velocity at the closest separation than the effect of Γ_1. The reason for this is that the maximum density for the neutron star mass of $1.35M_\odot$ is not so large that their structure depends weakly on Γ_1, which determines the stiffness of the core EOS.

Figure 16 compares the binding energy of an equal-mass binary neutron star with that of an unequal-mass one. The EOS we choose here is the piecewise polytrope with $\Gamma_1 = 3.0$ and $\log_{10} P_1 = 13.45$ (PwPoly30-1345). The thick (red) dashed curve denotes the result for an equal-mass binary with $M_{\rm ADM}^{\rm NS1} = M_{\rm ADM}^{\rm NS2} = 1.35\,M_\odot$, while the thick (blue) dot-dashed one is for an unequal-mass binary composed of $M_{\rm ADM}^{\rm NS1} = 1.15M_\odot$ and $M_{\rm ADM}^{\rm NS2} = 1.55\,M_\odot$ stars. The thin (black) solid and thin (green) dotted curves are the results of the 3PN approximation for the equal-mass and unequal-mass binaries, respectively. When the mass ratio decreases to the value as small as $1.15\,M_\odot/1.55\,M_\odot \simeq 0.74$, the fractional binding energy $E_{\rm b}/M_0$ and orbital angular velocity $M_0\Omega$ at the closest separation decrease by about 10%. The reason why the orbital angular velocity at the closest separation decreases for the unequal-mass case is that the less massive star is tidally deformed by the more massive companion star and

Table 2
Selected Data of Spherical Stars with Piecewise Polytropic EOSs, Tabulated Realistic EOSs, and Fitted EOSs

EOS Name	$M_{\rm ADM}^{\rm NS}$ ($M_\odot$)	$M_{\rm B}$ ($M_\odot$)	$R_{\rm NS}$ (km)	$a_{\rm NS}$ (km)	$\mathcal{C}$	ρ_c (g cm^{-3})	ϵ_c
PwPoly30-1395	1.150	1.225	15.08	13.33	0.1126	3.378(+14)	1.048
	1.250	1.339	15.16	13.25	0.1218	3.560(+14)	1.053
	1.350	1.455	15.23	13.16	0.1309	3.743(+14)	1.058
	1.450	1.572	15.28	13.05	0.1401	3.930(+14)	1.063
	1.550	1.691	15.32	12.93	0.1494	4.124(+14)	1.068
	2.835	3.409	13.37	8.677	0.3131	1.085(+15)	1.425
PwPoly30-1355	1.150	1.245	12.23	10.47	0.1388	6.234(+14)	1.065
	1.250	1.363	12.26	10.33	0.1505	6.623(+14)	1.072
	1.350	1.484	12.28	10.18	0.1624	7.027(+14)	1.079
	1.450	1.607	12.27	10.02	0.1744	7.461(+14)	1.088
	1.550	1.732	12.26	9.835	0.1867	7.925(+14)	1.098
	2.249	2.700	10.62	6.903	0.3126	1.724(+15)	1.429
PwPoly30-1345	1.150	1.250	11.59	9.821	0.1465	7.294(+14)	1.070
	1.250	1.370	11.61	9.674	0.1590	7.770(+14)	1.078
	1.350	1.493	11.61	9.509	0.1718	8.274(+14)	1.087
	1.450	1.617	11.59	9.326	0.1847	8.821(+14)	1.097
	1.550	1.745	11.55	9.120	0.1981	9.418(+14)	1.110
	2.122	2.547	10.03	6.523	0.3123	1.934(+15)	1.429
PwPoly30-1335	1.150	1.257	10.98	9.200	0.1547	8.550(+14)	1.076
	1.250	1.378	10.98	9.038	0.1681	9.140(+14)	1.085
	1.350	1.502	10.96	8.856	0.1819	9.775(+14)	1.096
	1.450	1.629	10.93	8.652	0.1960	1.048(+15)	1.108
	1.550	1.759	10.87	8.421	0.2106	1.126(+15)	1.124
	2.003	2.402	9.475	6.163	0.3121	2.169(+15)	1.429
PwPoly30-1315	1.150	1.271	9.814	8.026	0.1730	1.184(+15)	1.091
	1.250	1.397	9.783	7.828	0.1887	1.277(+15)	1.104
	1.350	1.525	9.728	7.604	0.2049	1.383(+15)	1.119
	1.450	1.657	9.643	7.346	0.2220	1.507(+15)	1.139
	1.550	1.794	9.515	7.040	0.2406	1.659(+15)	1.166
	1.783	2.136	8.449	5.501	0.3117	2.732(+15)	1.431
PwPoly27-1345	1.150	1.247	11.69	9.919	0.1453	7.782(+14)	1.079
	1.250	1.367	11.64	9.706	0.1586	8.439(+14)	1.089
	1.350	1.489	11.57	9.471	0.1723	9.168(+14)	1.101
	1.450	1.614	11.47	9.208	0.1866	9.984(+14)	1.116
	1.550	1.742	11.35	8.911	0.2017	1.093(+15)	1.134
	1.926	2.261	9.709	6.557	0.2929	2.175(+15)	1.410
PwPoly27-1335	1.150	1.255	10.91	9.133	0.1557	9.521(+14)	1.088
	1.250	1.377	10.84	8.898	0.1703	1.040(+15)	1.100
	1.350	1.501	10.74	8.634	0.1856	1.139(+15)	1.116
	1.450	1.629	10.61	8.335	0.2017	1.255(+15)	1.135
	1.550	1.761	10.44	7.985	0.2193	1.398(+15)	1.160
	1.799	2.111	9.078	6.134	0.2926	2.489(+15)	1.410
PwPoly24-1345	1.150	1.242	11.83	10.06	0.1436	8.567(+14)	1.092
	1.250	1.362	11.66	9.722	0.1584	9.609(+14)	1.107
	1.350	1.485	11.45	9.349	0.1741	1.084(+15)	1.126
	1.450	1.610	11.19	8.919	0.1914	1.238(+15)	1.150
	1.550	1.739	10.84	8.396	0.2111	1.448(+15)	1.185
	1.701	1.946	9.427	6.679	0.2665	2.477(+15)	1.383
PwPoly24-1335	1.150	1.252	10.76	8.980	0.1578	1.132(+15)	1.108
	1.250	1.375	10.55	8.601	0.1750	1.291(+15)	1.128
	1.350	1.501	10.27	8.158	0.1940	1.495(+15)	1.155
	1.450	1.631	9.894	7.602	0.2164	1.788(+15)	1.197
	1.566	1.790	8.690	6.160	0.2661	2.918(+15)	1.384
APR	1.150	1.248	11.37	9.601	0.1493	8.091(+14)	1.079
	1.250	1.368	11.36	9.429	0.1624	8.519(+14)	1.086
	1.350	1.491	11.35	9.249	0.1756	8.962(+14)	1.094
	1.450	1.616	11.33	9.059	0.1890	9.433(+14)	1.103
	1.550	1.745	11.29	8.856	0.2027	9.937(+14)	1.114
	2.189	2.658	9.932	6.285	0.3254	1.908(+15)	1.454
BBB2	1.150	1.248	11.31	9.538	0.1501	8.685(+14)	1.086
	1.250	1.369	11.25	9.317	0.1640	9.389(+14)	1.097
	1.350	1.492	11.18	9.075	0.1783	1.016(+15)	1.109
	1.450	1.618	11.08	8.807	0.1933	1.101(+15)	1.124
	1.550	1.748	10.95	8.507	0.2090	1.198(+15)	1.142

Table 2
(Continued)

EOS Name	$M_{\rm ADM}^{\rm NS}$ ($M_\odot$)	$M_{\rm B}$ ($M_\odot$)	$R_{\rm NS}$ (km)	$a_{\rm NS}$ (km)	$\mathcal{C}$	ρ_c (g cm^{-3})	ϵ_c
	1.920	2.267	9.506	6.355	0.2983	2.242(+15)	1.419
BPAL12	1.350	1.485	10.45	8.334	0.1908	1.698(+15)	1.191
	1.455	1.622	9.021	6.700	0.2381	2.928(+15)	1.357
FPS	1.150	1.250	11.06	9.287	0.1535	9.338(+14)	1.090
	1.250	1.372	10.99	9.054	0.1679	1.013(+15)	1.102
	1.350	1.496	10.90	8.797	0.1828	1.102(+15)	1.116
	1.450	1.623	10.78	8.507	0.1986	1.210(+15)	1.134
	1.550	1.754	10.62	8.168	0.2156	1.345(+15)	1.158
	1.800	2.103	9.279	6.343	0.2865	2.419(+15)	1.400
GNH3	1.150	1.221	14.47	12.72	0.1173	4.838(+14)	1.072
	1.250	1.336	14.37	12.46	0.1284	5.227(+14)	1.079
	1.350	1.453	14.26	12.19	0.1398	5.749(+14)	1.090
	1.450	1.572	14.12	11.88	0.1517	6.409(+14)	1.103
	1.550	1.693	13.92	11.52	0.1644	7.193(+14)	1.119
	1.964	2.228	11.38	8.223	0.2549	1.749(+15)	1.366
SLy4	1.150	1.243	11.83	10.07	0.1435	7.582(+14)	1.080
	1.250	1.363	11.80	9.864	0.1565	8.089(+14)	1.088
	1.350	1.484	11.75	9.652	0.1697	8.631(+14)	1.098
	1.450	1.609	11.69	9.423	0.1832	9.255(+14)	1.110
	1.550	1.736	11.60	9.171	0.1973	9.928(+14)	1.123
	2.049	2.429	9.986	6.614	0.3030	2.008(+15)	1.427
fitAPR	1.150	1.248	11.42	9.649	0.1487	7.980(+14)	1.078
	1.250	1.368	11.41	9.477	0.1617	8.418(+14)	1.085
	1.350	1.491	11.40	9.298	0.1749	8.877(+14)	1.094
	1.450	1.616	11.37	9.106	0.1883	9.362(+14)	1.103
	1.550	1.744	11.34	8.901	0.2019	9.884(+14)	1.114
	2.184	2.649	9.923	6.285	0.3250	1.915(+15)	1.456
fitFPS	1.150	1.251	10.98	9.205	0.1546	9.571(+14)	1.091
	1.250	1.373	10.91	8.966	0.1692	1.037(+15)	1.103
	1.350	1.497	10.81	8.705	0.1844	1.129(+15)	1.118
	1.450	1.625	10.69	8.413	0.2003	1.236(+15)	1.136
	1.550	1.756	10.53	8.074	0.2175	1.369(+15)	1.160
	1.799	2.105	9.233	6.295	0.2878	2.435(+15)	1.401
fitSLy4	1.150	1.243	11.76	9.994	0.1443	7.792(+14)	1.082
	1.250	1.363	11.72	9.785	0.1575	8.316(+14)	1.090
	1.350	1.485	11.66	9.565	0.1709	8.881(+14)	1.100
	1.450	1.609	11.59	9.330	0.1847	9.495(+14)	1.112
	1.550	1.737	11.51	9.074	0.1989	1.018(+15)	1.126
	2.042	2.423	9.915	6.552	0.3042	2.029(+15)	1.429

starts shedding mass at a larger separation than that for the equal-mass case. The binding energy decreases for the unequal-mass case because it is proportional to the reduced mass $\mu \equiv M_{\rm ADM}^{\rm NS1} M_{\rm ADM}^{\rm NS2}/M_0$ according to the results of the 3PN approximation (the ratio of the unequal-mass case to the equal-mass one is $\mu_{\rm uneq}/\mu_{\rm eq} \simeq 0.978$) and the orbital angular velocity at the termination point of the sequence should be smaller.

In Figure 17, the total angular momentum for the same models as in Figure 16 is shown along both equal-mass and unequal-mass sequences. The sequence of the total angular momentum for the unequal-mass case is located below that of the equal-mass case at the same orbital angular velocity. This is also because the total angular momentum is proportional to the reduced mass, according to the results of the 3PN approximation. However, because the orbital angular velocity at the termination point of the sequence is smaller for the unequal-mass case, its total angular momentum is approximately the same value as that for the equal-mass case coincidentally.

Finally, we show the effect of the total mass of binary neutron stars on the binding energy in Figure 18. The EOS we choose for this figure is one of the tabulated realistic EOSs, the APR

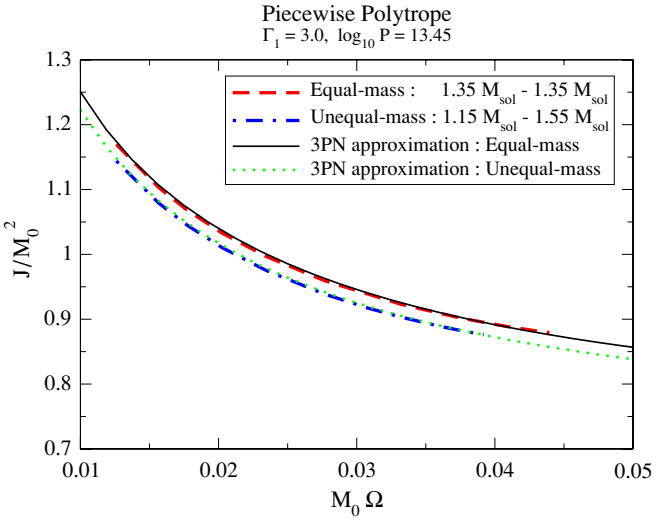

Figure 17. Same as Figure 16 but for the total angular momentum.
(A color version of this figure is available in the online journal.)

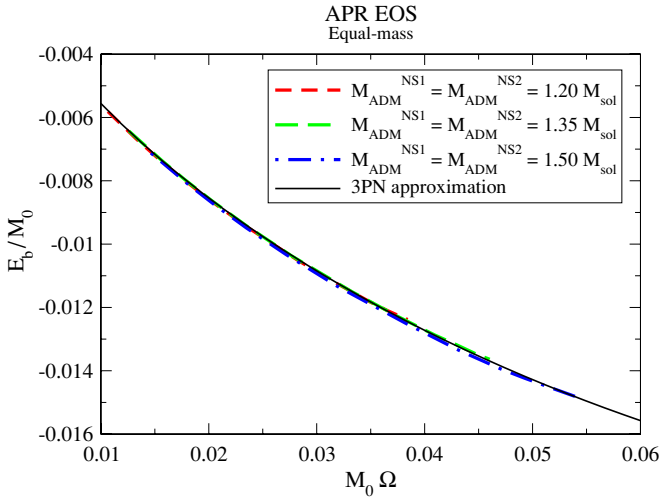

Figure 18. Same as Figure 13 but for the APR EOS. The thick (red) short-dashed, thick (green) long-dashed, and thick (blue) dot-dashed curves denote the results of equal-mass binary neutron stars with the total mass of $M_0 = 2.4\,M_\odot$, $2.7\,M_\odot$, and $3.0\,M_\odot$, respectively. The thin (black) solid curve denotes the results of the 3PN approximation.

(A color version of this figure is available in the online journal.)

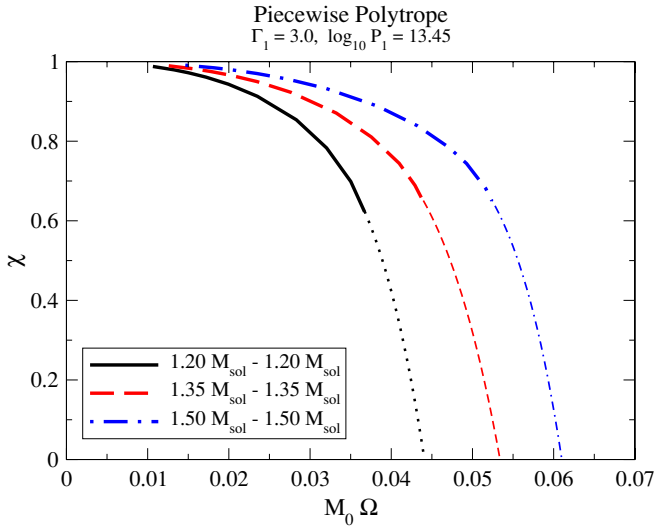

Figure 19. Mass-shedding indicator χ as a function of the orbital angular velocity. The EOS we select is the piecewise polytrope with $\Gamma_1 = 3.0$ and $\log_{10} P_1 = 13.45$ (PwPoly30-1345), and sequences of the equal-mass case are shown. The thick (black) solid, thick (red) dashed, and thick (blue) dot-dashed curves denote the computed sequences for equal-mass binary neutron stars with masses of $M_{\rm ADM}^{\rm NS1} = M_{\rm ADM}^{\rm NS2} = 1.20\,M_\odot$, $1.35\,M_\odot$, and $1.50\,M_\odot$, respectively. The thin (black) dotted, thin (red) dashed, and thin (blue) dot-dashed curves denote the extrapolated curves.

(A color version of this figure is available in the online journal.)

EOS. Figure 18 shows the results for three total masses, $2.4\,M_\odot$, $2.7\,M_\odot$, and $3.0\,M_\odot$. As the neutron star mass increases, the star becomes more compact and less subject to tidal disruption. For a binary system composed of more massive neutron stars, it is necessary that the two stars come closer to each other to reach their mass-shedding limit. This makes the orbital angular velocity at the mass-shedding limit increase for binary systems with massive neutron stars. Because of this effect, the orbital angular velocity at the closest separation is about 0.038 for $M_0 = 2.4\,M_\odot$ whereas it is about 0.054 for $M_0 = 3.0\,M_\odot$. We can understand this behavior by using Equation (61). By substituting each total mass and circumferential radius, we obtain the ratio of the orbital angular velocity as

$$\frac{(M_{\rm tot}\Omega)_{2.4\,M_\odot}}{(M_{\rm tot}\Omega)_{3.0\,M_\odot}} \simeq \left(\frac{2.4\,M_\odot/11.37\,{\rm km}}{3.0\,M_\odot/11.31\,{\rm km}}\right)^{3/2} \simeq 0.71. \qquad (64)$$

The actual ratio of the orbital angular velocity at the closest separation we obtained is

$$\frac{(M_0\Omega)_{2.4\,M_\odot}}{(M_0\Omega)_{3.0\,M_\odot}} \simeq \frac{0.038}{0.054} \simeq 0.70. \qquad (65)$$

This value agrees again with the estimated ratio given in Equation (64).

4.3. Endpoint of Sequences

We construct quasi-equilibrium sequences for three cases of total mass, three mass ratios for each total mass, and 18 EOSs. For all the sequences, we do not find the turning point of the binding energy and total angular momentum, which represents the innermost stable circular orbit of the binary system. Instead, the sequences terminate at the mass-shedding limit of a less massive star. (For equal-mass binaries, two neutron stars reach the mass-shedding limit at the same time.) As explained before, we stop constructing the sequences at $\chi \sim 0.6$ because our spectral method code cannot handle a cusp-like figure which appears at the mass-shedding limit. This implies that the closest separation with the largest value of $M_0\Omega$ we can calculate is not the actual endpoint of the sequence.

To determine the orbital angular velocity at the mass-shedding limit, we extrapolate a curve of the mass-shedding indicator χ as a function of $M_0\Omega$. The procedure is as follows: we first make a fitting polynomial equation of χ as a function of $M_0\Omega$ for sequences. Then, we extrapolate the fitting polynomial equation to $\chi = 0$ and determine the value of $M_0\Omega$ at $\chi = 0$. The extrapolated value of $M_0\Omega$ at $\chi = 0$ is defined as $M_0\Omega_{\rm ms}$. Figure 19 shows such extrapolated curves for the piecewise polytropic EOS with $\Gamma_1 = 3.0$ and $\log_{10} P_1 = 13.45$ (PwPoly30-1345). The thick (black) solid, thick (red) dashed, and thick (blue) dot-dashed curves denote the computed sequences for equal-mass binary neutron stars with masses of $M_{\rm ADM}^{\rm NS1} = M_{\rm ADM}^{\rm NS2} = 1.20\,M_\odot$, $1.35M_\odot$, and $1.50\,M_\odot$, respectively. The thin (black) dotted, thin (red) dashed, and thin (blue) dot-dashed curves denote the extrapolated curves.

For unequal-mass binaries, we apply the same method of extrapolation to less massive stars which will be tidally disrupted by their companion more massive stars. Figure 20 shows the sequences and extrapolated curves for unequal-mass binary neutron stars for the piecewise polytropic EOS with $\Gamma_1 = 3.0$ and $\log_{10} P_1 = 13.45$ (PwPoly30-1345). The (black) solid, (red) dashed, and (blue) dot-dashed curves denote the computed sequences with masses of $M_{\rm ADM}^{\rm NS1}$ versus $M_{\rm ADM}^{\rm NS2} = 1.00\,M_\odot$ versus $1.40\,M_\odot$, $1.15\,M_\odot$ versus $1.55\,M_\odot$, and $1.30\,M_\odot$ versus $1.70\,M_\odot$, respectively. For each curve, the thick and thin ones denote the sequences for less massive stars and those for more massive ones, respectively. The thin (black) dotted, thin (red) dot-dash-dashed, and thin (blue) dot-dot-dashed curves are the extrapolated ones.

The estimated orbital angular velocity at the mass-shedding limit is by about 20% larger than that at the closest separation we can calculate for each sequence where the less massive star has $\chi \sim 0.6$. The orbital angular velocity at the mass-shedding limit computed by the extrapolation is summarized in Appendix C.

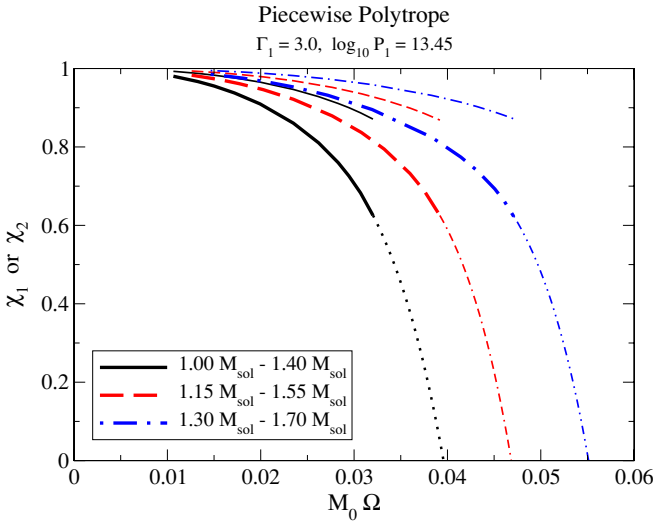

Figure 20. Same as Figure 19 but for unequal-mass models. The (black) solid, (red) dashed, and (blue) dot-dashed curves denote the computed sequences with masses of $M_{\rm ADM}^{\rm NS1}$ vs. $M_{\rm ADM}^{\rm NS2} = 1.00\,M_\odot$ vs. $1.40\,M_\odot$, $1.15\,M_\odot$ vs. $1.55\,M_\odot$, and $1.30\,M_\odot$ vs. $1.70\,M_\odot$, respectively. For each curve above, the thick and thin ones denote the sequences for less massive stars and those for more massive ones, respectively. The thin (black) dotted, thin (red) dot-dash-dashed, and thin (blue) dot-dot-dashed curves are the extrapolated ones.

(A color version of this figure is available in the online journal.)

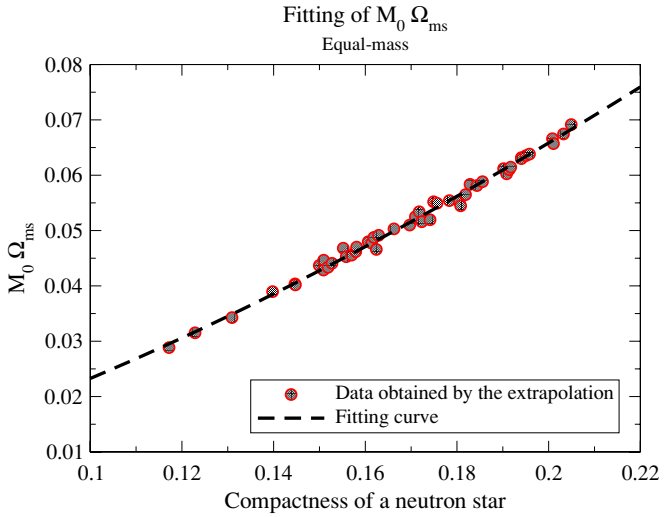

Figure 21. Fitting curve for the equal-mass models. The filled (red) circles denote the orbital angular velocity at the mass-shedding limit obtained by our extrapolation method as a function of the compactness of a neutron star. The (black) dashed curve is the fitting curve for the data.

(A color version of this figure is available in the online journal.)

Let us continue investigating the orbital angular velocity at the mass-shedding limit, $M_0\Omega_{\rm ms}$. By regarding the Newtonian quantities, $M_{\rm tot}$, $M_{\rm NS1}$, $M_{\rm NS2}$, and $r_{\rm NS1}$, in Equation (61) as the relativistic ones, M_0, $M_{\rm ADM}^{\rm NS1}$, $M_{\rm ADM}^{\rm NS2}$, and $R_{\rm NS1}$, where $R_{\rm NS1}$ is the circumferential radius of the less massive star, we can write $M_0\Omega_{\rm ms}$ by an empirical formula as

$$M_0\Omega_{\rm ms} = B\mathcal{C}_{\rm NS1}^{3/2}\left(1+\frac{1}{q}\right)^{3/2} q^{1/2}, \qquad (66)$$

where $q \equiv M_{\rm ADM}^{\rm NS1}/M_{\rm ADM}^{\rm NS2} \leqslant 1$ is the mass ratio, $\mathcal{C}_{\rm NS1} \equiv M_{\rm ADM}^{\rm NS1}/R_{\rm NS1}$ is the compactness of the less massive neutron star, and $B \equiv (1/A)^{3/2}$ is a constant. Figure 21 plots all equal-mass data as a function of the compactness of a neutron star, and we perform the fitting procedure by assuming the form of Equation (66). By this fitting, we determine the value of constant as $B \simeq 0.260$. Note here that we do not find any evidence that the value of B depends on the EOS. In other words, the value of $M_0\Omega_{\rm ms}$ depends only on the compactness of a neutron star, and only weakly on the EOSs.

Figure 22 shows the results of fitting of $M_0\Omega_{\rm ms}$ for unequal-mass binaries as a function of the compactness of a less massive neutron star. For the fitting, we use the form of Equation (66) and determine the constant B for each mass ratio. The obtained values are $B \simeq 0.268$ for the case of $1.10M_\odot$ versus $1.30\,M_\odot$ ($q \simeq 0.846$), $B \simeq 0.275$ for $1.00\,M_\odot$ versus $1.40\,M_\odot$ ($q \simeq 0.714$), $B \simeq 0.270$ for $1.25\,M_\odot$ versus $1.45\,M_\odot$ ($q \simeq 0.862$), $B \simeq 0.273$ for $1.15\,M_\odot$ versus $1.55\,M_\odot$ ($q \simeq 0.742$), $B \simeq 0.268$ for $1.40\,M_\odot$ versus $1.60\,M_\odot$ ($q = 0.875$), and $B \simeq 0.279$ for $1.30\,M_\odot$ versus $1.70M_\odot$ ($q \simeq 0.765$). Even though the value B depends weakly on the mass ratio, i.e., the case of smaller q tends to have a larger B, we suppose that the dependence comes from the error of extrapolation because the deviation of B from its averaged value, 0.270, is about 3%. We would like to remind that the estimated orbital angular velocity at the mass-shedding limit is about 20% larger than that at the closest separation we can calculate: the error of 3% could be produced by a slight

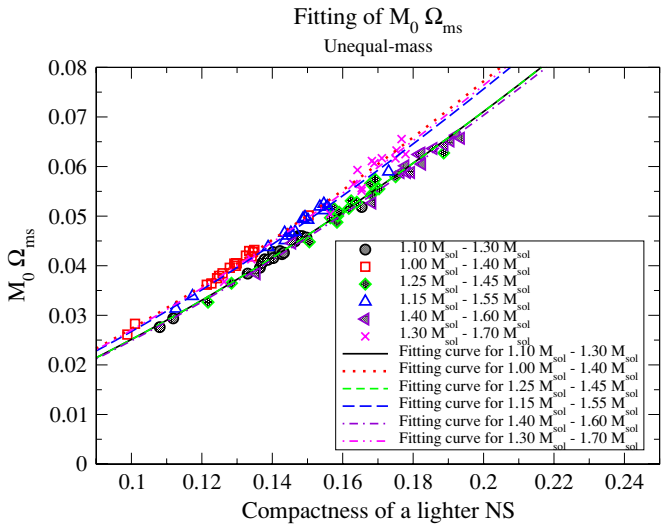

Figure 22. Same as Figure 21 but for unequal-mass models. Filled (black) circles, open (red) squares, filled (green) diamonds, open (blue) up-triangles, filled (violet) left-triangles, and (magenta) crosses denote, respectively, the orbital angular velocity at the mass-shedding limit for models of $1.10\,M_\odot$ vs. $1.30\,M_\odot$, $1.00\,M_\odot$ vs. $1.40\,M_\odot$, $1.25\,M_\odot$ vs. $1.45\,M_\odot$, $1.15\,M_\odot$ vs. $1.55\,M_\odot$, $1.40\,M_\odot$ vs. $1.60\,M_\odot$, and $1.30\,M_\odot$ vs. $1.70\,M_\odot$. The (black) solid, (red) dotted, (green) short-dashed, (blue) long-dashed, (violet) dot-dashed, and (magenta) dot-dot-dashed curves are the fitting curves for the data.

(A color version of this figure is available in the online journal.)

change in the extrapolation curve. From the results for the mass ratio $0.71 < q \leqslant 1$, we conclude that the constant B which appears in Equation (66) can be set to $B = 0.270$.

The value of $B = 0.270$ is slightly larger than that derived for Newtonian close binaries (Paczyński 1971). If we translate the constant in Paczyński (1971) for an equal-mass binary, it becomes $B = 0.38^{3/2} \simeq 0.23$; our result is about 17% larger. On the other hand, the value of $B = 0.270$ we obtained is the same as that found for quasi-equilibrium sequences of black hole-neutron star binaries in general relativity in Taniguchi et al. (2008). In addition, Shibata & Uryū (2006, 2007) give the same value for a black hole-neutron star binary in general relativity

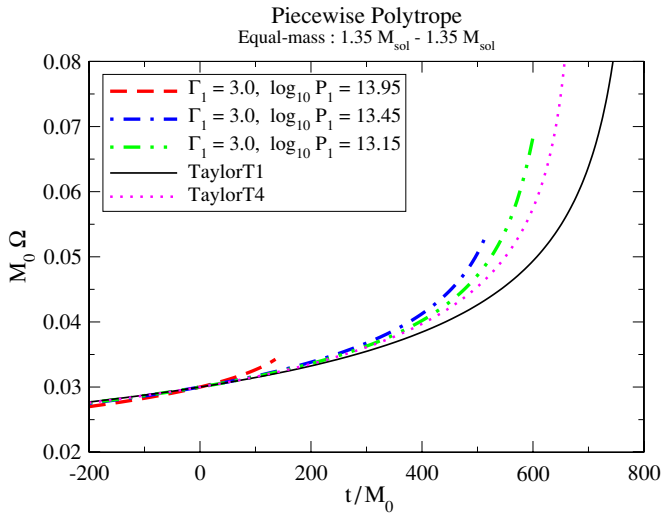

Figure 23. Orbital angular velocity as a function of time for equal-mass binary neutron stars each with a mass of 1.35 $M_\odot$. All the EOSs are the piecewise polytrope with $\Gamma_1 = 3.0$ but have different values of $\log_{10} P_1$. The thick (red) dashed, thick (blue) dot-dashed, and thick (green) dot-dot-dashed curves denote the cases of $\log_{10} P_1 = 13.95$ (PwPoly30-1395), 13.45 (PwPoly30-1345), and 13.15 (PwPoly30-1315), respectively. The thin (black) solid and thin (magenta) dotted curves are calculated by using TaylorT1 and TaylorT4 in Boyle et al. (2007).

(A color version of this figure is available in the online journal.)

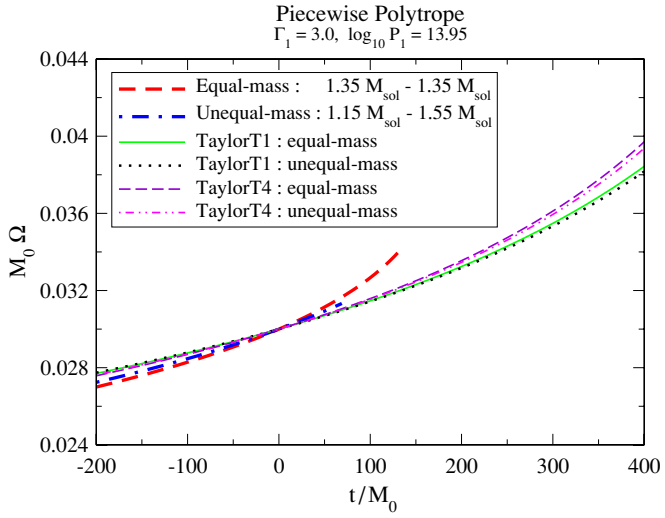

Figure 24. Same as Figure 23 but for the piecewise polytrope with $\Gamma_1 = 3.0$ and $\log_{10} P_1 = 13.95$ (PwPoly30-1395) and for comparing the results of equal-mass with unequal-mass binaries. The thick (red) dashed and thick (blue) dot-dashed curves respectively denote the cases of equal-mass binary, each with a mass of 1.35 $M_\odot$ and those of unequal-mass binary with masses of 1.15 $M_\odot$ and 1.55 $M_\odot$. The thin (green) solid and thin (black) dotted curves are calculated by using TaylorT1 in Boyle et al. (2007) for equal-mass binary and unequal-mass one of mass ratio, 1.15/1.55. The thin (violet) dashed and thin (magenta) dot-dot-dashed curves are for TaylorT4 in Boyle et al. (2007).

(A color version of this figure is available in the online journal.)

where the neutron star is corotating. The value of $B = 0.270$ with Equation (66) could be widely used as an estimation of the orbital angular velocity at the mass-shedding limit for neutron stars in a relativistic binary system.

4.4. Quasi-stationary Evolution of the Orbital Angular Velocity

As we stated in Section 1, one of the primary purposes for constructing quasi-equilibrium states is to provide initial data

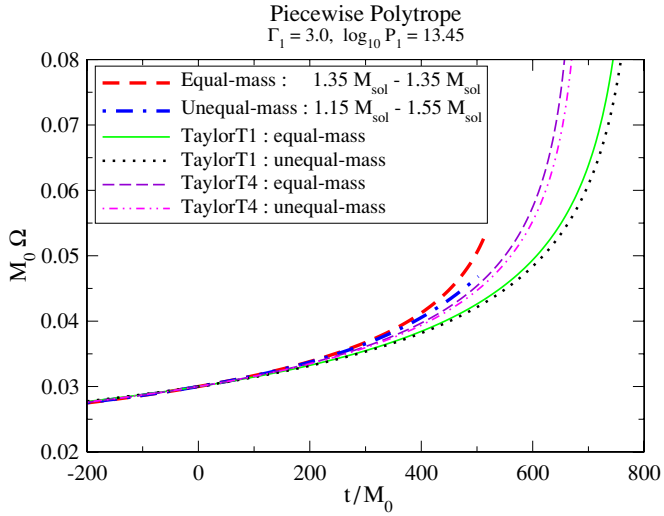

Figure 25. Same as Figure 24 but for $\Gamma_1 = 3.0$ and $\log_{10} P_1 = 13.45$ (PwPoly30-1345).

(A color version of this figure is available in the online journal.)

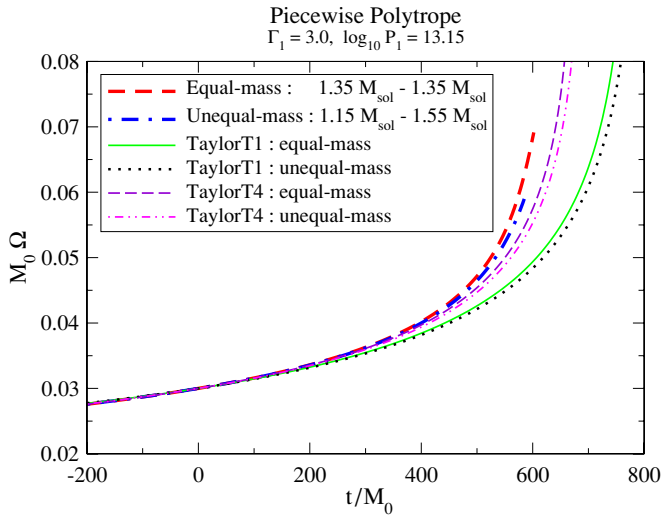

Figure 26. Same as Figure 24 but for $\Gamma_1 = 3.0$ and $\log_{10} P_1 = 13.15$ (PwPoly1315).

(A color version of this figure is available in the online journal.)

for inspiral and merger simulations in numerical relativity. It will be quite useful for numerical relativity community, if we provide quantities with which they can compare the results of simulations in the inspiral phase. One of the quantities derived from quasi-equilibrium results is the time evolution of the orbital angular velocity. To obtain the orbital angular velocity as a function of time, we adopt a similar method introduced by Boyle et al. (2007). Assuming the quasi-stationary adiabatic evolution of the inspiral orbit, we may write the time derivative of the orbital angular velocity as

$$\frac{d\Omega}{dt} = \frac{dE/dt}{dE/d\Omega} \equiv F(\Omega)^{-1}. \tag{67}$$

This equation is the same as Equation (55) in Uryū et al. (2009). For the temporal change in the binding energy of the binary neutron stars, dE/dt, we use the 3.5PN equation shown in Blanchet (2006). On the other hand, we estimate the change in the binding energy, $dE/d\Omega$, as follows: we write the binding

Table 3
Quasi-equilibrium Sequence Data for the Polytropic EOS with $\Gamma = 2$

$\bar{d}$	d/M_0	$M_0\Omega$	E_b/M_0	J/M_0^2	χ_1	$\delta\chi$ or χ_2	δM
			$\bar{M}_B = 0.15$ vs. 0.15				
4.872	17.46	1.270(−2)	−6.481(−3)	1.1675	0.9755	8.375(−10)	1.285(−5)
4.263	15.28	1.535(−2)	−7.294(−3)	1.1094	0.9612	1.812(−9)	1.403(−5)
3.959	14.19	1.705(−2)	−7.779(−3)	1.0795	0.9499	3.374(−9)	1.463(−5)
3.654	13.10	1.909(−2)	−8.331(−3)	1.0490	0.9336	7.775(−9)	1.572(−5)
3.350	12.01	2.156(−2)	−8.964(−3)	1.0179	0.9093	2.219(−8)	1.894(−5)
3.045	10.91	2.463(−2)	−9.692(−3)	0.9865	0.8705	1.182(−8)	2.438(−5)
2.862	10.26	2.684(−2)	−1.018(−2)	0.9676	0.8347	4.197(−8)	3.673(−5)
2.680	9.605	2.939(−2)	−1.073(−2)	0.9487	0.7816	5.520(−9)	8.642(−5)
2.497	8.950	3.239(−2)	−1.132(−2)	0.9306	0.6902	1.243(−8)	1.433(−4)
2.375	8.513	3.473(−2)	−1.171(−2)	0.9186	0.5562	4.544(−9)	1.348(−4)
			$\bar{M}_B = 0.14$ vs. 0.16				
4.872	17.47	1.269(−2)	−6.454(−3)	1.1635	0.9668	0.9826	1.438(−5)
4.263	15.29	1.534(−2)	−7.264(−3)	1.1056	0.9476	0.9724	1.618(−5)
3.959	14.20	1.704(−2)	−7.747(−3)	1.0758	0.9322	0.9643	1.729(−5)
3.654	13.11	1.907(−2)	−8.297(−3)	1.0454	0.9100	0.9527	1.911(−5)
3.350	12.01	2.154(−2)	−8.927(−3)	1.0144	0.8762	0.9356	2.397(−5)
3.045	10.92	2.461(−2)	−9.653(−3)	0.9832	0.8210	0.9087	3.211(−5)
2.862	10.27	2.681(−2)	−1.014(−2)	0.9644	0.7668	0.8846	4.867(−5)
2.741	9.829	2.847(−2)	−1.050(−2)	0.9518	0.7154	0.8634	8.845(−5)
2.619	9.392	3.031(−2)	−1.087(−2)	0.9397	0.6349	0.8353	1.165(−4)
2.558	9.174	3.132(−2)	−1.107(−2)	0.9336	0.5703	0.8175	1.291(−4)
			$\bar{M}_B = 0.13$ vs. 0.17				
4.872	17.51	1.265(−2)	−6.371(−3)	1.1516	0.9562	0.9886	1.451(−5)
4.263	15.32	1.530(−2)	−7.169(−3)	1.0943	0.9307	0.9817	1.675(−5)
3.959	14.22	1.699(−2)	−7.646(−3)	1.0648	0.9101	0.9763	1.829(−5)
3.654	13.13	1.902(−2)	−8.190(−3)	1.0348	0.8801	0.9687	2.149(−5)
3.350	12.04	2.149(−2)	−8.810(−3)	1.0043	0.8337	0.9573	2.955(−5)
3.167	11.38	2.324(−2)	−9.223(−3)	0.9858	0.7918	0.9478	3.376(−5)
3.045	10.94	2.455(−2)	−9.521(−3)	0.9736	0.7534	0.9398	4.321(−5)
2.923	10.50	2.597(−2)	−9.846(−3)	0.9611	0.7026	0.9303	7.790(−5)
2.832	10.18	2.714(−2)	−1.009(−2)	0.9521	0.6491	0.9215	9.314(−5)
2.741	9.847	2.841(−2)	−1.035(−2)	0.9430	0.5696	0.9109	1.086(−4)

Table 4
Quasi-equilibrium Sequence Data for the Piecewise Polytropic EOSs, the Tabulated Realistic EOSs, and the EOSs with a Fitting Formula

EOS Name	M_0	M_{ADM}^{NS1} vs. M_{ADM}^{NS2}	d/M_0	$M_0\Omega$	E_b/M_0	J/M_0^2	χ_1	$\delta\chi$ or χ_2	δM
				Piecewise polytropic EOSs					
PwPoly30-1395	2.4 $M_\odot$	1.20 $M_\odot$ vs. 1.20 $M_\odot$	22.57	8.788(−3)	−5.137(−3)	1.2952	0.9763	7.598(−11)	1.528(−6)
			19.75	1.065(−2)	−5.801(−3)	1.2267	0.9626	6.139(−11)	3.168(−6)
			18.34	1.185(−2)	−6.200(−3)	1.1912	0.9517	1.166(−10)	4.497(−6)
			16.93	1.328(−2)	−6.657(−3)	1.1549	0.9359	5.224(−11)	6.882(−6)
			15.52	1.504(−2)	−7.183(−3)	1.1178	0.9122	1.532(−10)	1.252(−5)
			14.11	1.722(−2)	−7.792(−3)	1.0801	0.8738	1.578(−10)	2.245(−5)
			13.26	1.880(−2)	−8.208(−3)	1.0574	0.8376	1.038(−10)	4.047(−5)
			12.70	1.999(−2)	−8.508(−3)	1.0423	0.8039	1.902(−12)	6.155(−5)
			11.85	2.205(−2)	−8.985(−3)	1.0203	0.7269	8.396(−11)	1.025(−4)
			11.15	2.411(−2)	−9.369(−3)	1.0031	0.6040	1.677(−10)	7.167(−5)

(This table is available in its entirety in a machine-readable form in the online journal. A portion is shown here for guidance regarding its form and content.)

energy as

$$E_b = (E)_{3.5PN} + ax^5 + bx^6 + cx^7, \tag{68}$$

where $x \equiv (M_0\Omega)^{2/3}$, and $(E)_{3.5PN}$ denotes the binding energy through 3.5PN order. The constants, a, b, and c, are determined by numerically fitting the obtained sequences. Then we calculate the change in the binding energy by taking the derivative with respect to the orbital angular velocity as

$$\frac{dE}{d\Omega} = \frac{d}{d\Omega}E_b. \tag{69}$$

By numerically integrating Equation (67), we obtain the orbital angular velocity as a function of time,

$$t = \int_{\Omega_{ini}}^{\Omega_{fin}} F(\Omega)d\Omega. \tag{70}$$

Table 5
Quasi-equilibrium Sequence Data for the Piecewise Polytropic EOSs Calculated by the Old Code

EOS Name	d/M_0	$M_0\Omega$	E_b/M_0	J/M_0^2	χ_1	$\delta\chi$	δM
			$M_0 = 2.7\,M_\odot$ (1.35 $M_\odot$ vs. 1.35 $M_\odot$)				
PwPoly30-1395	20.06	1.042(−2)	−5.716(−3)	1.2349	0.9777	7.312(−11)	2.312(−5)
	17.56	1.261(−2)	−6.445(−3)	1.1712	0.9647	6.789(−13)	2.364(−5)
	16.30	1.402(−2)	−6.883(−3)	1.1382	0.9543	4.033(−11)	2.397(−5)
	15.05	1.571(−2)	−7.382(−3)	1.1046	0.9393	1.640(−12)	2.436(−5)
	13.79	1.777(−2)	−7.954(−3)	1.0703	0.9168	7.662(−12)	2.480(−5)
	12.54	2.032(−2)	−8.615(−3)	1.0355	0.8807	2.144(−12)	2.527(−5)
	11.79	2.218(−2)	−9.057(−3)	1.0146	0.8471	2.353(−11)	2.553(−5)
	11.29	2.358(−2)	−9.372(−3)	1.0008	0.8161	2.248(−10)	2.565(−5)
	10.53	2.600(−2)	−9.860(−3)	0.9808	0.7461	7.776(−11)	2.815(−5)
	9.782	2.891(−2)	−1.036(−2)	0.9625	0.6083	8.829(−13)	1.793(−5)
PwPoly30-1355	17.56	1.261(−2)	−6.345(−3)	1.1713	0.9862	2.181(−11)	7.871(−5)
	15.05	1.570(−2)	−7.286(−3)	1.1040	0.9764	8.569(−12)	7.501(−5)
	13.79	1.776(−2)	−7.866(−3)	1.0692	0.9680	1.342(−11)	7.214(−5)
	12.54	2.030(−2)	−8.540(−3)	1.0337	0.9552	3.733(−11)	6.837(−5)
	11.29	2.352(−2)	−9.331(−3)	0.9974	0.9346	5.479(−12)	6.322(−5)
	10.03	2.769(−2)	−1.027(−2)	0.9607	0.8986	1.116(−10)	5.505(−5)
	9.280	3.084(−2)	−1.091(−2)	0.9388	0.8623	5.875(−11)	4.818(−5)
	8.778	3.329(−2)	−1.136(−2)	0.9244	0.8266	2.272(−10)	4.204(−5)
	8.026	3.768(−2)	−1.207(−2)	0.9041	0.7351	6.037(−11)	2.576(−5)
	7.524	4.122(−2)	−1.254(−2)	0.8923	0.6058	2.536(−10)	2.027(−5)
PwPoly30-1345	17.56	1.261(−2)	−6.376(−3)	1.1709	0.9894	4.763(−11)	4.829(−5)
	15.05	1.570(−2)	−7.320(−3)	1.1037	0.9818	2.422(−11)	5.201(−5)
	13.79	1.775(−2)	−7.901(−3)	1.0689	0.9753	3.826(−11)	5.480(−5)
	12.54	2.029(−2)	−8.577(−3)	1.0332	0.9654	3.836(−11)	5.855(−5)
	11.29	2.351(−2)	−9.372(−3)	0.9968	0.9496	6.109(−11)	6.303(−5)
	10.03	2.767(−2)	−1.031(−2)	0.9599	0.9225	3.944(−11)	6.359(−5)
	8.778	3.325(−2)	−1.143(−2)	0.9229	0.8705	2.735(−11)	5.800(−5)
	8.026	3.758(−2)	−1.219(−2)	0.9015	0.8107	4.171(−9)	4.860(−5)
	7.524	4.107(−2)	−1.270(−2)	0.8881	0.7439	8.933(−12)	3.411(−5)
	7.023	4.517(−2)	−1.320(−2)	0.8764	0.6095	1.665(−10)	4.469(−5)
PwPoly30-1335	17.56	1.262(−2)	−6.407(−3)	1.1711	0.9920	1.568(−11)	6.942(−6)
	15.05	1.571(−2)	−7.351(−3)	1.1039	0.9862	3.187(−11)	1.039(−5)
	13.79	1.776(−2)	−7.932(−3)	1.0690	0.9811	2.014(−11)	1.309(−5)
	12.54	2.030(−2)	−8.609(−3)	1.0332	0.9735	1.099(−11)	1.671(−5)
	11.29	2.351(−2)	−9.406(−3)	0.9967	0.9615	6.710(−11)	2.172(−5)
	10.03	2.767(−2)	−1.035(−2)	0.9595	0.9411	2.062(−12)	2.915(−5)
	8.778	3.323(−2)	−1.149(−2)	0.9220	0.9033	4.444(−11)	4.207(−5)
	8.026	3.754(−2)	−1.227(−2)	0.8999	0.8624	2.899(−12)	4.902(−5)
	7.023	4.500(−2)	−1.338(−2)	0.8724	0.7497	7.165(−11)	3.747(−5)
	6.521	4.979(−2)	−1.393(−2)	0.8609	0.5995	1.616(−9)	4.463(−5)
PwPoly30-1315	12.54	2.031(−2)	−8.663(−3)	1.0335	0.9854	7.983(−12)	7.350(−5)
	11.29	2.352(−2)	−9.461(−3)	0.9968	0.9786	4.702(−11)	6.898(−5)
	10.03	2.767(−2)	−1.041(−2)	0.9593	0.9673	1.884(−11)	6.251(−5)
	8.778	3.322(−2)	−1.156(−2)	0.9214	0.9468	1.995(−11)	5.273(−5)
	7.524	4.091(−2)	−1.295(−2)	0.8836	0.9051	9.948(−12)	3.645(−5)
	6.772	4.710(−2)	−1.390(−2)	0.8619	0.8556	1.887(−7)	2.042(−5)
	6.521	4.955(−2)	−1.421(−2)	0.8551	0.8303	2.438(−11)	1.992(−5)
	6.270	5.220(−2)	−1.455(−2)	0.8484	0.7979	5.634(−12)	9.248(−6)
	6.019	5.510(−2)	−1.488(−2)	0.8421	0.7535	2.232(−11)	2.958(−6)
	5.769	5.830(−2)	−1.519(−2)	0.8365	0.6822	1.244(−9)	2.976(−5)
PwPoly27-1345	17.56	1.262(−2)	−6.465(−3)	1.1711	0.9894	1.135(−12)	5.300(−5)
	15.05	1.571(−2)	−7.408(−3)	1.1039	0.9818	1.030(−10)	5.051(−5)
	13.79	1.776(−2)	−7.988(−3)	1.0690	0.9753	5.215(−11)	4.861(−5)
	12.54	2.030(−2)	−8.664(−3)	1.0333	0.9654	4.492(−13)	4.610(−5)
	11.29	2.351(−2)	−9.459(−3)	0.9968	0.9497	6.381(−12)	4.256(−5)
	10.03	2.767(−2)	−1.040(−2)	0.9598	0.9229	1.780(−11)	3.729(−5)
	8.778	3.325(−2)	−1.153(−2)	0.9227	0.8718	3.761(−11)	2.875(−5)
	8.026	3.757(−2)	−1.229(−2)	0.9010	0.8139	3.856(−8)	2.055(−5)
	7.524	4.104(−2)	−1.282(−2)	0.8872	0.7488	3.069(−11)	1.487(−5)
	7.023	4.510(−2)	−1.334(−2)	0.8748	0.6220	6.351(−10)	1.348(−5)
PwPoly27-1335	17.56	1.262(−2)	−6.462(−3)	1.1714	0.9927	1.984(−11)	6.815(−5)
	15.05	1.571(−2)	−7.406(−3)	1.1041	0.9873	2.861(−11)	6.626(−5)
	12.54	2.030(−2)	−8.663(−3)	1.0334	0.9756	3.534(−11)	6.243(−5)
	11.29	2.351(−2)	−9.460(−3)	0.9968	0.9646	3.260(−11)	5.937(−5)

Table 5
(Continued)

EOS Name	d/M_0	$M_0\Omega$	E_b/M_0	J/M_0^2	χ_1	$\delta\chi$	δM
	10.03	2.767(−2)	−1.041(−2)	0.9595	0.9459	1.010(−11)	5.483(−5)
	8.778	3.323(−2)	−1.155(−2)	0.9219	0.9116	2.458(−11)	4.788(−5)
	8.026	3.753(−2)	−1.233(−2)	0.8995	0.8751	1.174(−11)	4.147(−5)
	7.274	4.289(−2)	−1.318(−2)	0.8780	0.8117	4.060(−12)	3.737(−5)
	6.772	4.722(−2)	−1.377(−2)	0.8646	0.7356	9.635(−12)	3.163(−5)
	6.396	5.101(−2)	−1.422(−2)	0.8556	0.6171	4.778(−10)	5.789(−6)
PwPoly24-1345	17.56	1.262(−2)	−6.400(−3)	1.1712	0.9897	2.027(−11)	4.727(−6)
	15.05	1.571(−2)	−7.344(−3)	1.1039	0.9823	2.414(−11)	7.000(−6)
	13.79	1.776(−2)	−7.925(−3)	1.0690	0.9760	1.211(−11)	8.746(−6)
	12.54	2.030(−2)	−8.601(−3)	1.0333	0.9665	1.529(−11)	1.017(−5)
	11.29	2.351(−2)	−9.397(−3)	0.9968	0.9514	5.580(−12)	1.116(−5)
	10.03	2.767(−2)	−1.034(−2)	0.9596	0.9256	2.222(−12)	1.185(−5)
	8.778	3.324(−2)	−1.147(−2)	0.9223	0.8771	2.218(−11)	1.162(−5)
	8.026	3.755(−2)	−1.225(−2)	0.9003	0.8232	1.652(−9)	1.071(−5)
	7.274	4.293(−2)	−1.307(−2)	0.8794	0.7206	3.800(−11)	4.368(−6)
	6.897	4.615(−2)	−1.350(−2)	0.8699	0.6067	1.599(−9)	2.153(−5)
PwPoly24-1335	17.56	1.263(−2)	−6.419(−3)	1.1719	0.9941	4.219(−12)	4.160(−5)
	15.05	1.572(−2)	−7.362(−3)	1.1044	0.9896	1.890(−11)	3.917(−5)
	12.54	2.031(−2)	−8.621(−3)	1.0335	0.9800	1.687(−11)	3.488(−5)
	11.29	2.352(−2)	−9.420(−3)	0.9968	0.9709	8.805(−12)	3.134(−5)
	10.03	2.767(−2)	−1.037(−2)	0.9594	0.9557	3.814(−11)	2.622(−5)
	8.778	3.322(−2)	−1.152(−2)	0.9215	0.9282	2.864(−11)	1.870(−5)
	8.026	3.751(−2)	−1.231(−2)	0.8988	0.8997	6.863(−13)	1.218(−5)
	7.023	4.490(−2)	−1.350(−2)	0.8694	0.8292	1.460(−12)	5.031(−6)
	6.521	4.957(−2)	−1.413(−2)	0.8555	0.7620	1.019(−11)	4.111(−6)
	6.145	5.365(−2)	−1.462(−2)	0.8461	0.6651	1.809(−10)	2.280(−5)

Here $\Omega_{\rm ini}$ is the initial orbital angular velocity at which the time is defined to be zero, and $\Omega_{\rm fin}$ is the final orbital angular velocity. For $\Omega_{\rm fin}$, we use the orbital angular velocity at the mass-shedding limit obtained in Section 4.3.

Figure 23 shows the orbital angular velocity as a function of time for three piecewise polytropes with $\Gamma_1 = 3.0$. The thick (red) dashed, thick (blue) dot-dashed, and thick (green) dot-dot-dashed curves denote the results for $\log_{10} P_1 = 13.95$ (PwPoly30-1395), 13.45 (PwPoly30-1345), and 13.15 (PwPoly30-1315), respectively. All of them are calculated by using the equal-mass sequences of $M_{\rm ADM}^{\rm NS1} = M_{\rm ADM}^{\rm NS2} = 1.35\,M_\odot$. We also show two reference curves of TaylorT1 and TaylorT4 introduced by Boyle et al. (2007). The initial orbital angular velocity is set to $M_0\Omega_{\rm ini} = 0.03$. It is found that the curve of the most compact neutron stars (the dot-dot-dashed curve, PwPoly30-1315) is the closest to that of TaylorT4 among all the models. This is reasonable because the neutron stars in this EOS are the most compact and tidal effects are the weakest. On the other hand, the curve of the least compact neutron stars (the dashed curve, PwPoly30-1395) has already deviated from the curves of TaylorT1 and TaylorT4 before reaching the initial orbital angular velocity $M_0\Omega_{\rm ini} = 0.03$, because of the tidal deformation. This shows that if we would like to compare the time evolution of the orbital angular velocity obtained by simulations, we need to start the simulations from a much smaller value of the orbital angular velocity for such less-compact neutron star models.

Figure 23 also shows that the quasi-equilibrium results are closer to those of TaylorT4 than those of TaylorT1, even though our calculation method of the orbital angular velocity as a function of time is similar to that of TaylorT1 (see Equation (67)). We, however, believe that at the limit of test mass, our method gives similar results of TaylorT1.

Figures 24–26 compare the results of unequal-mass binaries with those of equal-mass ones with the total mass of $M_0 = 2.7\,M_\odot$. The equal-mass binary has the mass of $M_{\rm ADM}^{\rm NS1} = M_{\rm ADM}^{\rm NS2} = 1.35\,M_\odot$, and the unequal-mass binary does $M_{\rm ADM}^{\rm NS1} = 1.15\,M_\odot$ and $M_{\rm ADM}^{\rm NS2} = 1.55\,M_\odot$. The EOSs are the same as those in Figure 23, but the results for $\log_{10} P_1 = 13.95$ (PwPoly30-1395), 13.45 (PwPoly30-1345), and 13.15 (PwPoly30-1315) are shown in Figures 24–26, respectively. From these figures, we find that the curves for unequal-mass binaries are located below those for equal-mass binaries for $t > 0$ and are closer to the post-Newtonian results, in particular for a less-compact neutron star model (see Figures 25 and 26). It is also found that the curves for unequal-mass binaries terminate before their deviation from the post-Newtonian results becomes larger. These two findings imply that even though the deformation of the less massive star is larger in the case of unequal-mass binaries than that in the equal-mass case when we compare at the same orbital angular velocity, the more massive star remains close to a spherical star and dominates the motion of binary system in the unequal-mass case. The effect of the deformation of stars on the orbital angular velocity is larger for the equal-mass binaries if the total mass is the same.

4.5. Comparison of the Results by Tabulated Realistic EOSs with Those by a Fitting Formula

Before closing Section 4, we would like to comment on the results by using the fitted EOSs. As shown in Figure 3, the mass–radius relation is very close to that for the tabulated realistic EOSs because we mimic them in constructing the fitting formula (Shibata et al. 2005; Shibata & Taniguchi 2006). As expected, the difference between the results for the fitted EOSs and those for the tabulated realistic EOSs is very small.

Even for the orbital angular velocity at the mass-shedding limit which is obtained by the extrapolation of sequences, the difference between the results of these two EOSs is less than about 5%.

5. SUMMARY

In the present paper, quasi-equilibrium sequences of binary neutron stars are constructed for 18 EOSs except for the $\Gamma = 2$ polytrope, in the IWM framework in general relativity. The EOSs we choose are nine piecewise polytropes, six tabulated realistic EOSs derived by using various theories of dense nuclear matter and different solution methods of the many-body problem in nuclear physics, and three EOSs expressed by a fitting formula. We employ three total masses, $M_0 = 2.4\,M_\odot$, $2.7\,M_\odot$, and $3.0\,M_\odot$ for each EOS, and compute sequences of three mass ratios for each total mass: i.e., $M_{\rm ADM}^{\rm NS1}$ versus $M_{\rm ADM}^{\rm NS2}$= $1.20\,M_\odot$ versus $1.20\,M_\odot$, $1.10\,M_\odot$ versus $1.30\,M_\odot$, and $1.00\,M_\odot$ versus $1.40\,M_\odot$ for $M_0 = 2.4\,M_\odot$; $1.35\,M_\odot$ versus $1.35\,M_\odot$, $1.25\,M_\odot$ versus $1.45\,M_\odot$, and $1.15\,M_\odot$ versus $1.55\,M_\odot$ for $M_0 = 2.7\,M_\odot$; and $1.50\,M_\odot$ versus $1.50\,M_\odot$, $1.40\,M_\odot$ versus $1.60\,M_\odot$, and $1.30\,M_\odot$ versus $1.70\,M_\odot$ for $M_0 = 3.0\,M_\odot$.

We focus on the unequal-mass sequences and compare their results with those of the equal-mass case. Changing the mass ratio, the total mass, and the EOSs, we investigate the behavior of the binding energy and total angular momentum along a sequence, the endpoint of sequences, and the orbital angular velocity as a function of time. For example, it is found for the piecewise polytropic EOSs that the change in stellar radius fixing the stiffness of the core EOS makes the orbital angular velocity at the mass-shedding limit vary widely, while the change in stiffness of the core EOS fixing the stellar radius does not change the orbital angular velocity at the mass-shedding limit significantly.

It is also found that the orbital angular velocity at the closest separation decreases as we decrease the mass ratio, $M_{\rm ADM}^{\rm NS1}/M_{\rm ADM}^{\rm NS2} \leqslant 1$. The reason is that the less massive star in an unequal-mass binary is tidally deformed by the companion more massive star and starts shedding mass at larger separation than that for the equal-mass case. It is found that the orbital angular velocity at the mass-shedding limit increases as the neutron star mass increases. This is because a more massive star becomes more compact and more difficult to be tidally disrupted for the same EOS. This implies that the binary neutron stars with massive stars need to come closer than those with less massive stars for reaching the mass-shedding limit. The orbital angular velocity at the mass-shedding limit is analyzed by using a Newtonian argument, and an empirical formula is found as

$$M_0\Omega_{\rm ms} = 0.270\mathcal{C}_{\rm NS1}^{3/2}\left(1+\frac{1}{q}\right)^{3/2} q^{1/2}. \qquad (71)$$

We have provided tables for 160 sequences as shown in Appendix B. Those tables may be useful as one of the database for future works on binary neutron stars in quasi-equilibrium and as a guideline of numerical simulations for the inspiral and merger.

We thank Charalampos Markakis and Koutarou Kyutoku for providing a list of parameters for the piecewise polytropic equations of state. We also thank John L. Friedman for useful comments. This work was supported in part by NSF Grant

Table 6
Orbital Angular Velocity at the Mass-shedding Limit

EOS Name	$M_0(M_\odot)$	$M_{\rm ADM}^{\rm NS1}(M_\odot)$	$M_{\rm ADM}^{\rm NS2}(M_\odot)$	$M_0\Omega_{\rm ms}$
Piecewise polytropic EOSs				
PwPoly30-1395	2.40	1.20	1.20	0.0289
		1.10	1.30	0.0276
		1.00	1.40	0.0261
	2.70	1.35	1.35	0.0343
		1.25	1.45	0.0326
		1.15	1.55	0.0313
	3.00	1.50	1.50	0.0402
		1.40	1.60	0.0384
		1.30	1.70	0.0367
PwPoly30-1355	2.40	1.20	1.20	0.0404
		1.10	1.30	0.0384
		1.00	1.40	0.0362
	2.70	1.35	1.35	0.0466
		1.25	1.45	0.0448
		1.15	1.55	0.0438
	3.00	1.50	1.50	0.0552
		1.40	1.60	0.0526
		1.30	1.70	0.0504
PwPoly30-1345	2.40	1.20	1.20	0.0441
		1.10	1.30	0.0415
		1.00	1.40	0.0396
	2.70	1.35	1.35	0.0534
		1.25	1.45	0.0508
		1.15	1.55	0.0468
	3.00	1.50	1.50	0.0610
		1.40	1.60	0.0588
		1.30	1.70	0.0551
PwPoly30-1335	2.40	1.20	1.20	0.0477
		1.10	1.30	0.0459
		1.00	1.40	0.0432
	2.70	1.35	1.35	0.0565
		1.25	1.45	0.0543
		1.15	1.55	0.0512
	3.00	1.50	1.50	0.0675
		1.40	1.60	0.0643
		1.30	1.70	0.0616
PwPoly30-1315	2.40	1.20	1.20	0.0545
		1.10	1.30	0.0518
		1.00	1.40	0.0501
	2.70	1.35	1.35	0.0692
		1.25	1.45	0.0627
		1.15	1.55	0.0590
PwPoly27-1345	2.40	1.20	1.20	0.0434
		1.10	1.30	0.0412
		1.00	1.40	0.0385
	2.70	1.35	1.35	0.0516
		1.25	1.45	0.0500
		1.15	1.55	0.0466
	3.00	1.50	1.50	0.0630
		1.40	1.60	0.0588
		1.30	1.70	0.0557
PwPoly27-1335	2.40	1.20	1.20	0.0491
		1.10	1.30	0.0460
		1.00	1.40	0.0428
	2.70	1.35	1.35	0.0588
		1.25	1.45	0.0555
		1.15	1.55	0.0520
	3.00	1.50	1.50	–
		1.40	1.60	0.0657
		1.30	1.70	0.0625
PwPoly24-1345	2.40	1.20	1.20	0.0429
		1.10	1.30	0.0396
		1.00	1.40	0.0364

Table 6
(Continued)

EOS Name	$M_0(M_\odot)$	$M_{\rm ADM}^{\rm NS1}(M_\odot)$	$M_{\rm ADM}^{\rm NS2}(M_\odot)$	$M_0\Omega_{\rm ms}$
	2.70	1.35	1.35	0.0520
		1.25	1.45	0.0488
		1.15	1.55	0.0451
	3.00	1.50	1.50	0.0666
		1.40	1.60	0.0605
PwPoly24-1335	2.40	1.20	1.20	0.0503
		1.10	1.30	0.0457
		1.00	1.40	0.0419
	2.70	1.35	1.35	0.0632
		1.25	1.45	0.0579
Tabulated realistic EOSs				
APR	2.40	1.20	1.20	0.0453
		1.10	1.30	0.0423
		1.00	1.40	0.0400
	2.70	1.35	1.35	0.0549
		1.25	1.45	0.0531
		1.15	1.55	0.0498
	3.00	1.50	1.50	0.0638
		1.40	1.60	0.0627
		1.30	1.70	0.0607
BBB2	2.40	1.20	1.20	0.0456
		1.10	1.30	0.0426
		1.00	1.40	0.0405
	2.70	1.35	1.35	0.0554
		1.25	1.45	0.0528
		1.15	1.55	0.0493
	3.00	1.50	1.50	0.0657
		1.40	1.60	0.0636
		1.30	1.70	0.0617
BPAL12	2.40	1.20	1.20	0.0470
		1.10	1.30	0.0428
	2.70	1.35	1.35	0.0603
FPS	2.40	1.20	1.20	0.0480
		1.10	1.30	0.0449
		1.00	1.40	0.0420
	2.70	1.35	1.35	0.0584
		1.25	1.45	0.0566
		1.15	1.55	0.0519
	3.00	1.50	1.50	–
		1.40	1.60	0.0652
		1.30	1.70	0.0632
GNH3	2.40	1.20	1.20	0.0315
		1.10	1.30	0.0294
		1.00	1.40	0.0283
	2.70	1.35	1.35	0.0390
		1.25	1.45	0.0365
		1.15	1.55	0.0339
	3.00	1.50	1.50	0.0462
		1.40	1.60	0.0446
		1.30	1.70	0.0413
SLy4	2.40	1.20	1.20	0.0437
		1.10	1.30	0.0406
		1.00	1.40	0.0375
	2.70	1.35	1.35	0.0510
		1.25	1.45	0.0497
		1.15	1.55	0.0466
	3.00	1.50	1.50	0.0612
		1.40	1.60	0.0588
		1.30	1.70	0.0565
EOSs with a fitting formula				
fitAPR	2.40	1.20	1.20	0.0468
		1.10	1.30	0.0430
		1.00	1.40	0.0404

Table 6
(Continued)

EOS Name	$M_0(M_\odot)$	$M_{\rm ADM}^{\rm NS1}(M_\odot)$	$M_{\rm ADM}^{\rm NS2}(M_\odot)$	$M_0\Omega_{\rm ms}$
	2.70	1.35	1.35	0.0552
		1.25	1.45	0.0516
		1.15	1.55	0.0494
	3.00	1.50	1.50	0.0635
		1.40	1.60	0.0624
		1.30	1.70	0.0611
fitFPS	2.40	1.20	1.20	0.0488
		1.10	1.30	0.0460
		1.00	1.40	0.0430
	2.70	1.35	1.35	0.0581
		1.25	1.45	0.0574
		1.15	1.55	0.0525
	3.00	1.50	1.50	–
		1.40	1.60	0.0663
		1.30	1.70	0.0655
fitSLy4	2.40	1.20	1.20	0.0446
		1.10	1.30	0.0413
		1.00	1.40	0.0379
	2.70	1.35	1.35	0.0525
		1.25	1.45	0.0516
		1.15	1.55	0.0461
	3.00	1.50	1.50	0.0615
		1.40	1.60	0.0601
		1.30	1.70	0.0593

PHY-0503366, and by Grant-in-Aid for Scientific Research (21340051) and for Scientific Research on Innovative Area (20105004) of the Japanese MEXT.

APPENDIX A

DATA OF SPHERICAL STARS

In Table 2, some selected data of spherical neutron stars is listed. In each table, the ADM mass $M_{\rm ADM}^{\rm NS}$, the baryon rest mass $M_{\rm B}$, the circumferential radius $R_{\rm NS}$, the coordinate radius $a_{\rm NS}$, the compactness $\mathcal{C} \equiv M_{\rm ADM}^{\rm NS}/R_{\rm NS}$, the central baryon rest-mass density ρ_c in cgs units, and the central specific internal energy ϵ_c are shown. The number in parentheses for ρ_c means the exponent of 10. For each EOS, we show the data at the maximum mass in the last line.

APPENDIX B

SEQUENCE DATA

The sequence data for the polytropic EOS with $\Gamma = 2$ is summarized in Table 3, that for the piecewise polytropic EOSs, the tabulated realistic EOSs, and the EOSs with a fitting formula in Table 4, and that for the piecewise polytropic EOSs calculated by the old code in Table 5. The coordinate separation d/M_0, the orbital angular velocity $M_0\Omega$, the binding energy $E_{\rm b}/M_0$, the total angular momentum J/M_0^2, the mass-shedding indicator for the less massive star χ_1, that for the more massive star χ_2, and the virial error δM are shown. For the sequences for the $\Gamma = 2$ polytrope, we additionally show the coordinate separation in polytropic units $\bar{d}$. For the sequences of equal-mass binaries, we only show the mass-shedding indicator for one neutron star χ_1 because the two stars are identical. However, because of numerical error there is a slight difference between the values of χ for two stars. Such a difference is described by

$\delta\chi \equiv |(\chi_1 - \chi_2)/\chi_1|$ in the tables for equal-mass binaries. The number in parentheses means the exponent of 10.

APPENDIX C

ORBITAL ANGULAR VELOCITY AT THE MASS-SHEDDING LIMIT

In Table 6, we summarize the orbital angular velocity at the mass-shedding limit which is estimated by using the extrapolation method described in Section 4.3. The orbital angular velocity is listed for each EOS and for each mass ratio. There are three cases for which we do not show the estimated value, i.e., for the cases of PwPoly27-1335, FPS, and fitFPS with masses of $1.50\,M_\odot$ versus $1.50\,M_\odot$. For those cases, we cannot calculate configurations for close separations, because both stars are compact and it is difficult to converge the computation. Since the mass-shedding indicator χ is still larger than 0.8 for those sequences at the closest separation we can calculate, the extrapolation method does not work well for estimating the orbital angular velocity at the mass-shedding limit.

REFERENCES

Acernese, F., et al. 2007, Class. Quantum Grav., 24, S381
Akmal, A., Pandharipande, V. R., & Ravenhall, D. G. 1998, Phys. Rev. C, 58, 1804
Anderson, M., Hirschmann, E. W., Lehner, L., Liebling, S. L., Motl, P. M., Neilsen, D., Palenzuela, C., & Tohline, J. E. 2008a, Phys. Rev. D, 77, 024006
Anderson, M., Hirschmann, E. W., Lehner, L., Liebling, S. L., Motl, P. M., Neilsen, D., Palenzuela, C., & Tohline, J. E. 2008b, Phys. Rev. Lett., 100, 191101
Ando, M., et al. 2005, Class. Quantum Grav., 22, S881
Asada, H. 1998, Phys. Rev. D, 57, 7292
Baiotti, L., Giacomazzo, B., & Rezzolla, L. 2008, Phys. Rev. D, 78, 084033
Baldo, M., Bombaci, I., & Burgio, G. F. 1997, A&A, 328, 274
Baumgarte, T. W., Cook, G. B., Scheel, M. A., Shapiro, S. L., & Teukolsky, S. A. 1997, Phys. Rev. Lett., 79, 1182
Baumgarte, T. W., Cook, G. B., Scheel, M. A., Shapiro, S. L., & Teukolsky, S. A. 1998, Phys. Rev. D, 57, 7299
Baumgarte, T. W., & Shapiro, S. L. 2003, Phys. Rep., 376, 41
Baumgarte, T. W., & Shapiro, S. L. 2009, Phys. Rev. D, 80, 064009
Baym, G., Pethik, C., & Sutherland, P. 1971, ApJ, 170, 299
Bejger, M., Gondek-Rosińska, D., Gourgoulhon, E., Haensel, P., Taniguchi, K., & Zdunik, J. L. 2005, A&A, 431, 297
Bildsten, L., & Cutler, C. 1992, ApJ, 400, 175
Blanchet, L. 2006, Living Rev. Rel., 9, 4
Bonazzola, S., Gourgoulhon, E., & Marck, J.-A. 1997, Phys. Rev. D, 56, 7740
Bonazzola, S., Gourgoulhon, E., & Marck, J.-A. 1999, Phys. Rev. Lett., 82, 892
Boyle, M., Brown, D. A., Kidder, L. E., Mroué, A. H., Pfeiffer, H. P., Scheel, M. A., Cook, G. B., & Teukolsky, S. A. 2007, Phys. Rev. D, 76, 124038
Brown, D. A., et al. 2004, Class. Quantum Grav., 21, S1625
Chamel, N., & Haensel, P. 2008, Living Rev. Rel., 11, 10
Cook, G. B. 2000, Living Rev. Rel., 3, 5
Douchin, F., & Haensel, P. 2001, A&A, 380, 151
Duez, M. D., Marronetti, P., Shapiro, S. L., & Baumgarte, T. W. 2003, Phys. Rev. D, 67, 024004
Friedman, B., & Pandharipande, V. R. 1981, Nucl. Phys. A, 361, 502
Giacomazzo, B., Rezzolla, L., & Baiotti, L. 2009, MNRAS, 399, L164
Glendenning, N. K. 1985, ApJ, 293, 470
Gourgoulhon, E. 2007, J. Phys.: Conf. Ser., 91, 012001
Gourgoulhon, E., Grandclément, P., Taniguchi, K., Marck, J.-A., & Bonazzola, S. 2001, Phys. Rev. D, 63, 064029
Haensel, P., & Pichon, B. 1994, A&A, 283, 313
Haensel, P., & Potekhin, A. Y. 2005, A&A, 428, 191
Isenberg, J. A. 1978, Waveless Approximation Theories of Gravity (College Park, MD: Univ. Maryland), arXiv:gr-qc/0702113v1
Isenberg, J. A. 2008, Int. J. Mod. Phys. D, 17, 265
Kiuchi, K., Sekiguchi, Y., Shibata, M., & Taiguchi, K. 2009, Phys. Rev. D, 80, 064037
Kiuchi, K., Sekiguchi, Y., Shibata, M., & Taiguchi, K. 2010, Phys. Rev. Lett., 104, 141101
Kochanek, C. S. 1992, ApJ, 398, 234
Liu, Y. T., Shapiro, S. L., Etienne, Z. B., & Taniguchi, K. 2008, Phys. Rev. D, 78, 024012
Lorimer, D. R. 2008, Living Rev. Rel., 11, 8
Lück, H., et al. 2006, Class. Quantum Grav., 23, S71
Marronetti, P., Mathews, G. J., & Wilson, J. R. 1998, Phys. Rev. D, 58, 107503
Marronetti, P., Mathews, G. J., & Wilson, J. R. 1999, Phys. Rev. D, 60, 087301
Marronetti, P., & Shapiro, S. L. 2003, Phys. Rev. D, 68, 104024
Miller, M., Gressman, P., & Suen, W.-M. 2004, Phys. Rev. D, 69, 064026
Narayan, R., Paczynski, B., & Piran, T. 1992, ApJ, 395, L83
Oechslin, R., & Janka, H.-T. 2007, Phys. Rev. Lett., 99, 121102
Oechslin, R., Janka, H.-T., & Marek, A. 2007, A&A, 467, 395
Paczyński, B. 1971, ARA&A, 9, 183
Pfeiffer, H. P., & York, J. W., Jr. 2003, Phys. Rev. D, 67, 044022
Read, J. S., Lackey, B. D., Owen, B. J., & Friedman, J. L. 2009, Phys. Rev. D, 79, 124032
Read, J. S., Markakis, C., Shibata, M., Uryū, K., Creighton, J. D. E., & Friedman, J. L. 2009, Phys. Rev. D, 79, 124033
Shibata, M. 1998, Phys. Rev. D, 58, 024012
Shibata, M. 1999, Phys. Rev. D, 60, 104052
Shibata, M., & Taniguchi, K. 2006, Phys. Rev. D, 73, 064027
Shibata, M., Taniguchi, K., & Uryū, K. 2003, Phys. Rev. D, 68, 084020
Shibata, M., Taniguchi, K., & Uryū, K. 2005, Phys. Rev. D, 71, 084021
Shibata, M., & Uryū, K. 2000, Phys. Rev. D, 61, 064001
Shibata, M., & Uryū, K. 2002, Prog. Theor. Phys., 107, 265
Shibata, M., & Uryū, K. 2006, Phys. Rev. D, 74, 121503
Shibata, M., & Uryū, K. 2007, Class. Quantum Grav., 24, S125
Shibata, M., Uryū, K., & Friedman, J. L. 2004, Phys. Rev. D, 70, 044044
Swesty, F. D. 1996, J. Comput. Phys., 127, 118
Taniguchi, K., Baumgarte, T. W., Faber, J. A., & Shapiro, S. L. 2006, Phys. Rev. D, 74, 041502
Taniguchi, K., Baumgarte, T. W., Faber, J. A., & Shapiro, S. L. 2007, Phys. Rev. D, 75, 084005
Taniguchi, K., Baumgarte, T. W., Faber, J. A., & Shapiro, S. L. 2008, Phys. Rev. D, 77, 044003
Taniguchi, K., & Gourgoulhon, E. 2002a, Phys. Rev. D, 65, 044027
Taniguchi, K., & Gourgoulhon, E. 2002b, Phys. Rev. D, 66, 104019
Taniguchi, K., & Gourgoulhon, E. 2003, Phys. Rev. D, 68, 124025
Teukolsky, S. A. 1998, ApJ, 504, 442
Tichy, W. 2009, Class. Quantum Grav., 26, 175018
Uryū, K., & Eriguchi, Y. 2000, Phys. Rev. D, 61, 124023
Uryū, K., Limousin, F., Friedman, J. L., Gourgoulhon, E., & Shibata, M. 2006, Phys. Rev. Lett., 97, 171101
Uryū, K., Limousin, F., Friedman, J. L., Gourgoulhon, E., & Shibata, M. 2009, Phys. Rev. D, 80, 124004
Uryū, K., Shibata, M., & Eriguchi, Y. 2000, Phys. Rev. D, 62, 104015
Usui, F., & Eriguchi, Y. 2002, Phys. Rev. D, 65, 064030
Usui, F., Uryū, K., & Eriguchi, Y. 2000, Phys. Rev. D, 61, 024039
Wilson, J. R., & Mathews, G. J. 1989, in Frontiers in Numerical Relativity, ed. C. R. Evans, L. S. Finn, & D. W. Hobill (Cambridge: Cambridge Univ. Press), 306
Yamamoto, T., Shibata, M., & Taniguchi, K. 2008, Phys. Rev. D, 78, 064054
Zuo, W., Bombaci, I., & Lombardo, U. 1999, Phys. Rev. C, 60, 024605